Lattice model for the Coulomb interacting chiral limit of magic-angle twisted bilayer graphene: Symmetries, obstructions, and excitations

Oskar Vafek[1,2,*] and Jian Kang[3,†]

[1]*National High Magnetic Field Laboratory, Tallahassee, Florida 32310, USA*

[2]*Department of Physics, Florida State University, Tallahassee, Florida 32306, USA*

[3]*School of Physical Science and Technology & Institute for Advanced Study, Soochow University, Suzhou 215006, China*

(Received 21 June 2021; accepted 16 August 2021; published 24 August 2021)

We revisit the localized Wannier state description of the twisted bilayer graphene, focusing on the chiral limit. We provide a simple method for constructing such two-dimensional exponentially localized—yet valley polarized—Wannier states, centered on the sites of the honeycomb lattice, paying particular attention to maintaining all the unobstructed symmetries. This includes the unitary particle-hole symmetry, and the combination of $C_2\mathcal{T}$ and the chiral particle-hole symmetry. The $C_2\mathcal{T}$ symmetry alone remains topologically obstructed and is not represented in a simple site-to-site fashion. We also analyze the gap and the dispersion of single particle and single hole excitations above a strong coupling ground state at integer fillings, which we find to be dominated by the on-site and the nearest-neighbor terms of a triangular lattice hopping model, with a minimum at the center of the moiré Brillouin zone. Finally, we use the insight gained from this real-space description to understand the dependence of the gap and the effective mass on the range of the screened Coulomb interaction.

DOI: 10.1103/PhysRevB.104.075143

I. INTRODUCTION

There is a not-uncommon sentiment that lattice models are *a priori* unsuitable for the study of the narrow bands of twisted bilayer graphene (TBG) due to the topological nature of the narrow bands, and that an extended state basis, such as Bloch or hybrid Wannier states, is preferable. On the other hand, because the narrow bands [1–6] as a whole within each valley carry a zero Chern number, the results of Brouder *et al.* [7] guarantee that the exponentially localized Wannier states can be constructed, unlike if the Chern number were nonzero. The problem is very similar to the one studied by Soluyanov and Vanderbilt [8], where they explicitly constructed exponentially localized Wannier states for the Z_2 nontrivial topological insulator whose Chern number of course vanishes. They also discovered that the nontrivial topological nature of the bands does provide an obstruction to the exponential localization of the Wannier states, *if* they also insist on simple on-site representation of the time reversal symmetry. For the example of the Kane and Mele model with two sites per unit cell and two pairs of bands separated by a nontrivial gap, the exponentially localized Wannier states for the two lower bands, say, can be constructed. But if we insist that the action of the time reversal on the Wannier states simply results in another Wannier state within the orthonormal set spanning the isolated Hilbert space, then the Wannier states cannot be exponentially localized. If, instead, the two Wannier states are centered on different sites of the unit cell and so do not transform into each other under the time reversal, then there is no obstruction to exponential localization. It is often stated that the price to pay for the exponential localization is the breaking of the symmetry, which in the case of the two-dimensional (2D) Z_2 topological insulator is the time reversal symmetry. But because the transformation between the Bloch states and the Wannier states is perfectly unitary, no information can be lost. This information includes symmetry. Thus, strictly speaking, time reversal symmetry cannot be broken by such a unitary transformation, but rather it is not explicit (or on-site) in such Wannier representation. In practice, this means that acting with a time reversal symmetry operator on an exponentially localized Wannier state will lead to a linear combination of Wannier states from its vicinity, with coefficients that decay exponentially with distance [9].

The situation is similar in the continuum models of magic-angle twisted bilayer graphene, whose narrow bands are taken to be completely valley decoupled, in which case they are topologically nontrivial [10–12]. In this case, exponentially localized states can be constructed [13,14], but if we insist on the explicit (on-site) implementation of both the valley $U(1)$ and $C_2\mathcal{T}$ symmetry for the narrow bands, then we find an obstruction. This obstruction was originally thought to be fragile and removable by the addition of trivial remote bands [15]. But, as was recently shown in Ref. [16], inclusion of the particle-hole symmetry P of the continuum Hamiltonian makes the topology stable, in that it is impossible to add trivial remote bands and maintain explicit representation of all approximate emergent symmetries while keeping exponential localization. In the chiral limit [17], there is an additional chiral particle-hole symmetry $\mathcal{C}$ which will also play a role in our Wannier construction and the representation of a spin-valley U(4) symmetry.

Although we agree that there is a clear utility of the Bloch [18–24] (or hybrid Wannier [25–27]) description, one of the goals of this paper is to demonstrate the practical benefits of the Wannier states as a complementary description of the

*vafek@magnet.fsu.edu

†jkang@suda.edu.cn

strong coupling physics of the narrow bands [28,29]. In particular, we use them to explain the (exact) dispersion of a single particle or a single hole added to a correlated insulator at an integer filling in the strong coupling limit [30,31] of the chiral limit model [17]. As was recently shown [30], the chiral limit is approached within the renormalization group treatment of the Coulomb interacting Bistritzer-MacDonald model (BM) [1] of the magic-angle twisted bilayer graphene.

Even though the $C_2\mathcal{T}$ symmetry is not explicit in our Wannier basis, we construct the Wannier basis such that the combination of the chiral particle-hole symmetry $\mathcal{C}$ and $C_2\mathcal{T}$ is explicit, as is P. The possibility to explicitly represent $P\mathcal{C}C_2\mathcal{T}$ was insightfully pointed out by Bernevig *et al.* in Ref. [32]. As we demonstrate below, the strong coupling spin-valley $U(4)$ symmetry, explicit in our Wannier basis, is indeed tied to $P\mathcal{C}C_2\mathcal{T}$ as stated in Ref. [32]. To this end, we use the projection method [33] to construct the exponentially localized Wannier states by identifying suitable trial states, whose symmetry is then imprinted in the Wannier states. Usually, one follows the projection method with a maximal localization procedure that minimizes $\langle \delta \mathbf{r}^2 \rangle$, but for our trial states, it is not obvious that this second step provides a sufficient advantage and therefore we omit it.

The strong coupling dispersion curves can certainly be obtained numerically without much difficulty using the Bloch basis, but it is not easy to understand their shape. Our goal is to demonstrate that the real-space Wannier description provides a complementary way to understand it as a result of a tight-binding model on a moiré *triangular lattice*, with rapidly decaying hopping amplitudes as the hopping range is increased [34]. Note that the centers of the Wannier states are still on the honeycomb lattice sites *AB* and *BA* as in Refs. [13,14]. The triangular lattice tight-binding description of the one-particle strong coupling dispersion is a result of decoupling of the two (triangular) sublattices of the honeycomb lattice in the chiral limit.

The negative sign of the nearest-neighbor hopping amplitude, which can also be understood from the real-space description, then explains why the minimum of the dispersion is at the $\mathbf{\Gamma}$ point [center of the moiré Brillouin zone (mBZ)]. In addition, this method allows us to understand the dependence of the shape of these bands on the range of the interaction, controlled by the distance ξ to the grounded metallic screening layers, one placed above and another symmetrically below the twisted bilayer graphene. We find that once $\xi \gtrsim L_m$, where L_m is the moiré period, the effective mass of the excitations is nearly ξ independent even though the excitation gap still grows with increasing ξ (see Fig. 2). This can be understood by analyzing the effective electrostatics of the exchange and the direct contribution to the single particle dispersion. The direct term corresponds to an electrostatic energy of a localized "fidget spinner," whose shape is shown in Fig. 4(a), interacting with a moiré *periodic* charge distribution, thus probing the interaction potential $V_{\mathbf{q}}$ only at (nonzero) discrete reciprocal lattice wave vectors. Because the smallest such wave vector has a length $|\mathbf{g}_{1,2}| = 4\pi/(\sqrt{3}L_m) \approx 7.26/L_m$, the factor of $\tanh \frac{|\mathbf{g}_{1,2}|\xi}{2}$ in the two gate screened interaction $V_{\mathbf{q}} = \frac{2\pi e^2}{\epsilon|\mathbf{q}|} \tanh(\frac{|\mathbf{q}|\xi}{2})$ is not very sensitive to ξ for $\xi \gtrsim L_m$. This explains the ξ insensitivity shown in Fig. 2(b) for $\xi \gtrsim L_m$. In contrast, the exchange term corresponds to the electrostatic energy of *two localized* charge distributions, and thus probes the interaction at a continuum of wave vectors, not just at the discrete reciprocal lattice. By normalization, only the Wannier states centered on the same site—with the fidget spinner shape—contain a monopole charge contribution which does not vanish at small wave vectors [see Fig. 6(a)]. The contribution of two fidget spinners to the exchange energy is therefore sensitive to small wave vector behavior of the interaction, which is the reason for the ξ dependence of the on-site term in the tight-binding expansion of the strong coupling dispersion seen in Fig. 7(a). On the other hand, the contribution to the hopping must contain at least one product of two Wannier states centered at different sites, whose multipole expansion generically starts with a dipole [see Figs. 4(b)–6(f)], vanishing at small wave vectors [see Figs. 6(b) and 6(c)]. The electrostatic energy is therefore much less sensitive to the small wave vector part of the interaction, and is therefore nearly independent of ξ once $\xi \gtrsim L_m$.

Another goal of this paper is to elucidate the connection between the strong coupling U(4) × U(4) symmetry [21] in the chiral limit, the spin-valley U(4) symmetry away from the chiral limit [21] but assuming P (dubbed nonchiral flat in Ref. [32]), and the local spin-valley U(4) symmetry explicit in the Wannier basis [35]. We demonstrate that the last two U(4) symmetries are indeed different subgroups of U(4) × U(4), as also pointed out in Ref. [32].

This paper is organized as follows: in Sec. II, we define the starting model and spell out the action of its symmetries on the energy and Chern Bloch basis of the narrow bands. In Sec. III, we analyze the Coulomb interactions in the Bloch basis, display the (nonchiral flat) spin-valley U(4) and (first chiral) U(4) × U(4) symmetries, and relate them. We also solve for the strong coupling spectrum of either a single particle or a single hole added to the strong coupling eigenstates at integer fillings using the Bloch basis. In Sec. IV, we build the exponentially localized Wannier states using the projection method and analyze the action of symmetries on the Wannier states; we also identify the spin-valley U(4) symmetry of the projected density operator explicit in the Wannier basis and relate it to the (first chiral) U(4) × U(4) symmetry. In Sec. V, we analyze the strong coupling dispersion of either a single particle or a single hole added to the strong coupling eigenstates at integer fillings in the Wannier basis, and find the rapidly converging tight-binding hopping amplitudes for this dispersion at each integer filling ν. As shown in Figs. 2(a) and 2(b), the results from the Bloch and Wannier analysis match. In Sec. VI, we analyze the dependence of the tight-binding parameters on ξ, the range of the interaction, and provide the electrostatics analogy to understand the direct and exchange contributions. Finally, Sec. VII is devoted to a summary and conclusions.

II. BISTRITZER-MACDONALD HAMILTONIAN AND ITS SYMMETRIES

At the valley $\mathbf{K}$, the effective continuum Hamiltonian is [1,17]

$$\hat{H}_{BM} = \begin{pmatrix} v_F \sigma_{\frac{\theta}{2}} \cdot \mathbf{p} & T(\mathbf{r}) \\ T^\dagger(\mathbf{r}) & v_F \sigma_{-\frac{\theta}{2}} \cdot \mathbf{p} \end{pmatrix}, \tag{1}$$

where the twisted Pauli matrices are $\sigma_{\frac{\theta}{2}} = e^{-\frac{i}{4}\theta\sigma_z}(\sigma_x, \sigma_y)e^{\frac{i}{4}\theta\sigma_z}$; they act in the sublattice space. The interlayer hopping functions are $T(\mathbf{r}) = \sum_{j=1}^{3} T_j e^{-i\mathbf{q}_j\cdot\mathbf{r}}$, where $\mathbf{q}_1 = k_\theta(0, -1)$, $\mathbf{q}_{2,3} = k_\theta(\pm\frac{\sqrt{3}}{2}, \frac{1}{2})$, $k_\theta = \frac{8\pi}{3a_0}\sin\frac{\theta}{2} = 4\pi/(3L_m)$, $a_0 \approx 0.246$ nm, L_m is the period of the moiré lattice, and

$$T_{j+1} = w_0 1_2 + w_1\left[\cos\left(\frac{2\pi}{3}j\right)\sigma_x + \sin\left(\frac{2\pi}{3}j\right)\sigma_y\right], \quad (2)$$

where 1_n is an $n \times n$ unit matrix. The Hamiltonian in the valley $\mathbf{K}'$ is related to $\mathbf{K}$ by spinless time reversal symmetry implemented by the complex conjugation.

We can absorb the phase in $\sigma_{\pm\frac{\theta}{2}}$ into the eigenstates using a unitary transformation [17] on the Hamiltonian,

$$\hat{H}'_{BM} = \begin{pmatrix} e^{\frac{i}{4}\theta\sigma_z} & 0 \\ 0 & e^{-\frac{i}{4}\theta\sigma_z} \end{pmatrix}\hat{H}_{BM}\begin{pmatrix} e^{-\frac{i}{4}\theta\sigma_z} & 0 \\ 0 & e^{\frac{i}{4}\theta\sigma_z} \end{pmatrix}. \quad (3)$$

In the chiral limit, $w_0/w_1 = 0$, this has no effect on $T(\mathbf{r})$. The eigenstates of the $\hat{H}'_{BM}$ can be written as

$$\Psi_{n,\mathbf{k}}(\mathbf{r}) = \sum_{\mathbf{g}} \frac{1}{\sqrt{N_{uc}A_{uc}}}\begin{pmatrix} A_{n,\mathbf{g}}(\mathbf{k}) \\ B_{n,\mathbf{g}}(\mathbf{k})e^{i\mathbf{q}_1\cdot\mathbf{r}} \end{pmatrix}e^{i\mathbf{k}\cdot\mathbf{r}}e^{i\mathbf{g}\cdot\mathbf{r}}, \quad (4)$$

where $\mathbf{g} = m_1\mathbf{g}_1 + m_2\mathbf{g}_2$ for integer $m_{1,2}$, $\mathbf{g}_1 = \mathbf{q}_2 - \mathbf{q}_3$, and $\mathbf{g}_2 = \mathbf{q}_3 - \mathbf{q}_1$ (see Fig. 1); N_{uc} is the number of unit moiré cells in the system (or, equivalently, the number of $\mathbf{k}$ points in the regular mesh of the first Brillouin zone), and the area of the unit cell is $A_{uc} = 8\pi^2/(3\sqrt{3}k_\theta^2)$. Note that with this definition, $\mathbf{k}$ is measured relative to the upper layer Dirac point. Therefore, inversion takes it to $-\mathbf{k} - \mathbf{q}_1$. The Fourier coefficients are normalized as $\sum_{\mathbf{g}} A^\dagger_{n,\mathbf{g}}(\mathbf{k})A_{n',\mathbf{g}}(\mathbf{k}) + B^\dagger_{n,\mathbf{g}}(\mathbf{k})B_{n',\mathbf{g}}(\mathbf{k}) = \delta_{nn'}$. The triangular moiré lattice is spanned by the primitive lattice vectors $\mathbf{L}_1 = L_m(\frac{\sqrt{3}}{2}, \frac{1}{2})$ and $\mathbf{L}_2 = L_m(0, 1)$.

Symmetries

As emphasized by Po *et al.* [10], the $\hat{H}_{BM}$ as well as $\hat{H}'_{BM}$ are invariant under the $C_2\mathcal{T}$ symmetry, i.e.,

$$C_2\mathcal{T}: \quad 1_2\sigma_x\hat{H}^{\prime *}_{BM}(-\mathbf{r})1_2\sigma_x = \hat{H}'_{BM}(\mathbf{r}), \quad (5)$$

where the two-by-two identity matrix 1_2 in $1_2\sigma_x$ acts in the layer space. This transformation does not change $\mathbf{k}$ (or n), and we choose the phase of $\Psi_{n,\mathbf{k}}(\mathbf{r})$ such that it is an eigenstate of $C_2\mathcal{T}$ with an eigenvalue $+1$, i.e.,

$$C_2\mathcal{T}: \quad 1_2\sigma_x\Psi^*_{n,\mathbf{k}}(-\mathbf{r}) = \Psi_{n,\mathbf{k}}(\mathbf{r}). \quad (6)$$

This fixes the $\Psi_{n,\mathbf{k}}(\mathbf{r})$ up to an overall sign. For the purposes of this paper, we will not need to fix the sign globally as we did in Ref. [25].

At a general twist angle away from the magic angle, the spectrum is nondegenerate everywhere in the mBZ except at the $\mathbf{K}_m$ and $\mathbf{K}'_m$ points even in the chiral limit [17] defined as $w_0/w_1 = 0$. At a magic angle—at the first of which $w_1/v_Fk_\theta = 0.585\,663\,558\,389\,55$ (see Ref. [36])—and in the chiral limit, the narrow bands of $\hat{H}_{BM}$ are exactly flat [17]. When we include the Coulomb interaction coupling to the remote bands within the renormalization group scheme, the perfect sublattice polarization of the narrow band Hilbert space remains, but the bands are no longer exactly flat [30].

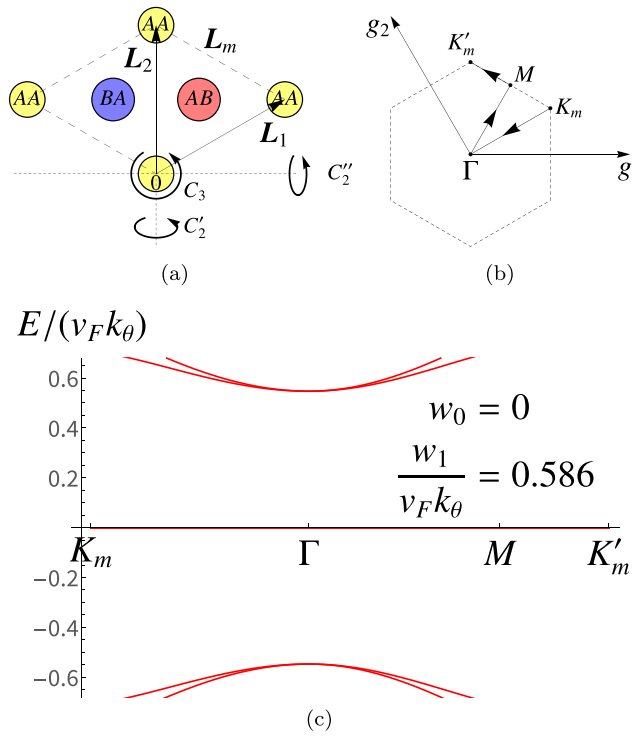

FIG. 1. (a) A unit cell of the triangular moiré lattice with the schematic of the *AA* stacking regions. The constructed Wannier states are centered on the *AB* and *BA* stacking regions, forming the dual honeycomb lattice. (b) The high symmetry path of the moiré Brillouin zone. (c) The narrow bands and a few remote bands in the chiral limit when $w_0 = 0$ and $w_1/(v_Fk_\theta) = 0.586$. The noninteracting energy in (c) is calculated from the BM model and expressed in units of v_Fk_θ.

For $w_0/w_1 = 0$, the $\hat{H}_{BM}$ and $\hat{H}'_{BM}$ enjoy the unitary chiral particle-hole symmetry [17],

$$\mathcal{C}: \quad \{1_2\sigma_z, \hat{H}'_{BM}\} = 0. \quad (7)$$

Therefore, if $\Psi_{n+,\mathbf{k}}(\mathbf{r})$ is an eigenstate of $\hat{H}'_{BM}$ with an eigenvalue $\epsilon_{n+,\mathbf{k}}$, then $1_2\sigma_z\Psi_{n+,\mathbf{k}}(\mathbf{r})$ is an eigenstate with an eigenvalue $-\epsilon_{n+,\mathbf{k}} = \epsilon_{n-,\mathbf{k}}$; the two eigenvalues are distinct unless we are exactly at a magic angle or $\mathbf{k} = \mathbf{K}_m, \mathbf{K}'_m$. This means that the linear combinations

$$\Phi_{\pm,\mathbf{k}}(\mathbf{r}) = \frac{1}{\sqrt{2}}(1_2\sigma_z \pm 1_4)\Psi_{n+,\mathbf{k}}(\mathbf{r}) \quad (8)$$

are perfectly sublattice polarized with $1_2\sigma_z$ eigenvalues ±1, and thus carry the Chern indices of ±1, respectively [17]. Note that Eq. (8) is well defined for both signs because $C_2\mathcal{T}$ anticommutes with $\mathcal{C}$, and we have already assumed (6). We also have

$$\mathcal{C}: \quad 1_2\sigma_z\Psi_{n+,\mathbf{k}}(\mathbf{r}) = e^{i\alpha^{\mathcal{C}}_{\mathbf{k}}}\Psi_{n-,\mathbf{k}}(\mathbf{r}), \quad (9)$$

where $\alpha^{\mathcal{C}}_{\mathbf{k}} = \pm\frac{\pi}{2}$, which can be obtained by acting on both sides with $C_2\mathcal{T}$ and using Eq. (6).

Because in the strong coupling limit, and near the magic angle, the Coulomb interaction exceeds the narrow bandwidth (containing two bands for each valley and spin), it

will generally mix the two bands. Therefore, it is a matter of convenience whether we choose the Chern basis $\Phi_{\pm,\mathbf{k}}(\mathbf{r})$, which diagonalizes $1_2\sigma_z$ for the narrow bands, or $\Psi_{n\pm,\mathbf{k}}(\mathbf{r})$, which diagonalizes $\hat{H}'_{BM}$.

As emphasized by Song *et al.* [11] and Hejazi *et al.* [37], $\hat{H}'_{BM}$ also enjoys another unitary particle-hole symmetry (see also Refs. [21,38]),

$$P:\ \begin{pmatrix} 0 & -1_2 \\ 1_2 & 0 \end{pmatrix}\hat{H}'_{BM}(-\mathbf{r})\begin{pmatrix} 0 & 1_2 \\ -1_2 & 0 \end{pmatrix} = -\hat{H}'_{BM}(\mathbf{r}). \quad (10)$$

Therefore, if $\Psi_{n,\mathbf{k}}(\mathbf{r})$ is an eigenstate of $\hat{H}'_{BM}$ with an eigenvalue $\epsilon_{n,\mathbf{k}}$, then $-i\mu_y 1_2\Psi_{n,\mathbf{k}}(-\mathbf{r})$ is an eigenstate at $-\mathbf{k}-\mathbf{q}_1$ with the eigenvalue $-\epsilon_{n,\mathbf{k}}$; the Pauli matrix μ_y acts in the layer space. This symmetry is approximately present even away from the chiral limit when the twist angle is small [12], and becomes exact if we ignore the rotation of the Pauli matrices in Eq. (1). Because the particle-hole symmetry P commutes with $C_2\mathcal{T}$ and because we already fixed the $C_2\mathcal{T}$ eigenvalue to $+1$ in Eq. (6), we have

$$P:\ -i\mu_y 1_2\Psi_{n+,\mathbf{k}}(-\mathbf{r}) = e^{i\alpha^P_{\mathbf{k}}}\Psi_{n-,-\mathbf{k}-\mathbf{q}_1}(\mathbf{r}), \quad (11)$$

where $\alpha^P_{\mathbf{k}} = 0,\pi$. We will find it convenient to fix the gauge such that

$$\alpha^P_{\mathbf{k}} = 0, \quad \forall \mathbf{k}\in \mathrm{mBZ}. \quad (12)$$

Then, at the $\boldsymbol{M}$ and $\boldsymbol{\Gamma}$ points, there are two independent ways to arrive at $\Psi_{n-,\mathbf{k}}$ starting from $\Psi_{n+,\mathbf{k}}$, either using Eq. (11) or using Eq. (9). At the $\boldsymbol{M}$ point ($\mathbf{k} = -\frac{\mathbf{q}_1}{2}$), numerically we find that these are consistent if $\alpha^{\mathcal{C}}_{\boldsymbol{M}} = -\frac{\pi}{2}$; we find the same result at the equivalent $\boldsymbol{M}$ points $\mathbf{k} = \frac{\mathbf{q}_{2,3}}{2}$. However, at the $\boldsymbol{\Gamma}$ point ($\mathbf{k} = \mathbf{q}_1$), we find $\alpha^{\mathcal{C}}_{\boldsymbol{\Gamma}} = \frac{\pi}{2}$.

We therefore use the remaining freedom to fix

$$\alpha^{\mathcal{C}}_{\mathbf{k}} = -\frac{\pi}{2}, \quad \mathbf{k}\neq\boldsymbol{\Gamma}, \quad (13)$$

$$\alpha^{\mathcal{C}}_{\mathbf{k}} = \frac{\pi}{2}, \quad \mathbf{k}=\boldsymbol{\Gamma}. \quad (14)$$

This locks the sign of $\Psi_{n+,-\mathbf{k}-\mathbf{q}_1}(\mathbf{r})$ to $\Psi_{n+,\mathbf{k}}(\mathbf{r})$ according to

$$\Psi_{n+,-\mathbf{k}-\mathbf{q}_1}(\mathbf{r}) = -\mu_y\sigma_z\Psi_{n+,\mathbf{k}}(-\mathbf{r}), \quad \mathbf{k}\neq\boldsymbol{\Gamma}, \quad (15)$$

$$\Psi_{n+,-\mathbf{k}-\mathbf{q}_1}(\mathbf{r}) = \mu_y\sigma_z\Psi_{n+,\mathbf{k}}(-\mathbf{r}), \quad \mathbf{k}=\boldsymbol{\Gamma}. \quad (16)$$

Therefore,

$$\mathcal{C}:\ 1_2\sigma_z\Phi_{\pm,\mathbf{k}}(\mathbf{r}) = \pm\Phi_{\pm,\mathbf{k}}(\mathbf{r}), \quad (17)$$

$$C_2\mathcal{T}:\ 1_2\sigma_x\Phi^*_{\pm,\mathbf{k}}(-\mathbf{r}) = -\Phi_{\mp,\mathbf{k}}(\mathbf{r}), \quad (18)$$

$$\begin{aligned} P:\ -i\mu_y 1_2\Phi_{\pm,\mathbf{k}}(-\mathbf{r}) &= \pm e^{i\alpha^P_{\mathbf{k}}}e^{-i\alpha^{\mathcal{C}}_{-\mathbf{k}-\mathbf{q}_1}}\Phi_{\pm,-\mathbf{k}-\mathbf{q}_1}(\mathbf{r}) \\ &= \pm e^{-i\alpha^{\mathcal{C}}_{-\mathbf{k}-\mathbf{q}_1}}\Phi_{\pm,-\mathbf{k}-\mathbf{q}_1}(\mathbf{r}). \end{aligned} \quad (19)$$

In addition, $\hat{H}'_{BM}$ is also invariant under the $C'_2\mathcal{T}$ and C_3 symmetries [10,13,14],

$$C'_2\mathcal{T}:\ \mu_x\hat{H}'^*_{BM}(-x,y)\mu_x = \hat{H}'_{BM}(x,y), \quad (20)$$

$$C_3:\ e^{-i\frac{\pi}{3}1_2\sigma_z}e^{-i\frac{2\pi}{3}\hat{\ell}_z}\hat{H}_{BM}e^{i\frac{2\pi}{3}\hat{\ell}_z}e^{i\frac{\pi}{3}1_2\sigma_z} = \hat{H}_{BM}, \quad (21)$$

where $\hat{\ell}_z = -i(x\frac{\partial}{\partial y} - y\frac{\partial}{\partial x})$. Because the spectrum is nondegenerate everywhere except at the $\mathbf{K}_m$ and $\mathbf{K}'_m$ points, the action of these symmetries maps the Bloch states at the related $\mathbf{k}$ points up to an overall phase.

The two valleys are related by (spinless) time reversal, i.e., by complex conjugation. The remaining symmetries can then be generated by the combination of the ones stated above.

III. COULOMB INTERACTIONS

The electron-electron Coulomb interactions, projected onto the narrow bands [30,32], are

$$\begin{aligned} H_{\mathrm{int}} &= \frac{1}{2}\int d^2\mathbf{r}d^2\mathbf{r}'V(\mathbf{r}-\mathbf{r}')\delta\rho(\mathbf{r})\delta\rho(\mathbf{r}') \\ &= \frac{1}{2N_{uc}A_{uc}}\sum_{\mathbf{q}}V_{\mathbf{q}}\sum_{\mathbf{R}\mathbf{R}'}e^{i\mathbf{q}\cdot(\mathbf{R}-\mathbf{R}')}\delta O^\dagger_{\mathbf{R}}(\mathbf{q})\delta O_{\mathbf{R}'}(\mathbf{q}), \end{aligned} \quad (22)$$

where

$$\delta\rho(\mathbf{r}) = \chi^\dagger_\sigma(\mathbf{r})\chi_\sigma(\mathbf{r}) - 2\sum_{\mathbf{k}}\sum_{n=n\pm}\Psi^\dagger_{n,\mathbf{k}}(\mathbf{r})\Psi_{n,\mathbf{k}}(\mathbf{r}),$$

$$V(\mathbf{r}) = \frac{1}{N_{uc}A_{uc}}\sum_{\mathbf{q}}V_{\mathbf{q}}e^{i\mathbf{q}\cdot\mathbf{r}}, \quad (23)$$

$$\delta O_{\mathbf{R}}(\mathbf{q}) = \int_{\mathrm{Wig.-Seitz}} d^2\mathbf{r}e^{-i\mathbf{q}\cdot\mathbf{r}}\delta\rho(\mathbf{R}+\mathbf{r}). \quad (24)$$

In the above, we are keeping only $V_{\mathbf{q}}$ with $|\mathbf{q}| \ll |\mathbf{K}|$, and thus neglecting the large wave vector transfer terms in the Coulomb interaction which are smaller by a factor $\sim L_m|\mathbf{K}|$ [39].

For a pure Coulomb interaction, we would have $V_{\mathbf{q}} = 2\pi e^2/(\epsilon q)$ except at $\mathbf{q}=\mathbf{0}$ where $V_{\mathbf{q}=\mathbf{0}} = 0$; in the later sections, we also study the two gate screened interactions, in which case $V_{\mathbf{q}\neq\mathbf{0}} = \frac{2\pi e^2}{\epsilon q}\tanh\frac{q\xi}{2}$. The projected field operators in Eq. (23) are expanded in the narrow band basis fermion annihilation operators $d_{\sigma,\mathbf{K}/\mathbf{K}',n,\mathbf{k}}$ as

$$\chi_\sigma(\mathbf{r}) = \begin{pmatrix}\psi_\sigma(\mathbf{r}) \\ \phi_\sigma(\mathbf{r})\end{pmatrix} = \sum_{\mathbf{k}}\sum_{n=n\pm}\begin{pmatrix}\Psi_{n,\mathbf{k}}(\mathbf{r})d_{\sigma,\mathbf{K},n,\mathbf{k}} \\ \Psi^*_{n,\mathbf{k}}(\mathbf{r})d_{\sigma,\mathbf{K}',n,-\mathbf{k}-\mathbf{q}_1}\end{pmatrix}. \quad (25)$$

The subscript σ refers to the electron spin projection $\uparrow$ or $\downarrow$.

If we now explicitly write out the projected density operator, using $C_2\mathcal{T}$ [Eq. (6)], P [Eq. (11)], and $\alpha^P_{\mathbf{k}} = 0$, we find that the terms from valley $\mathbf{K}$ and $\mathbf{K}'$ are related according to

$$\chi^\dagger_\sigma(\mathbf{r})\chi_\sigma(\mathbf{r}) = \sum_{\mathbf{k}\mathbf{k}'}(d^\dagger_{\sigma,\mathbf{K},+,\mathbf{k}}, d^\dagger_{\sigma,\mathbf{K},-,\mathbf{k}}, d^\dagger_{\sigma,\mathbf{K}',+,\mathbf{k}}, d^\dagger_{\sigma,\mathbf{K}',-,\mathbf{k}})\begin{pmatrix} A_{\mathbf{k}\mathbf{k}'}(\mathbf{r}) & B_{\mathbf{k}\mathbf{k}'}(\mathbf{r}) & 0 & 0 \\ C_{\mathbf{k}\mathbf{k}'}(\mathbf{r}) & D_{\mathbf{k}\mathbf{k}'}(\mathbf{r}) & 0 & 0 \\ 0 & 0 & D_{\mathbf{k}\mathbf{k}'}(\mathbf{r}) & -C_{\mathbf{k}\mathbf{k}'}(\mathbf{r}) \\ 0 & 0 & -B_{\mathbf{k}\mathbf{k}'}(\mathbf{r}) & A_{\mathbf{k}\mathbf{k}'}(\mathbf{r}) \end{pmatrix}\begin{pmatrix} d_{\sigma,\mathbf{K},+,\mathbf{k}'} \\ d_{\sigma,\mathbf{K},-,\mathbf{k}'} \\ d_{\sigma,\mathbf{K}',+,\mathbf{k}'} \\ d_{\sigma,\mathbf{K}',-,\mathbf{k}'}\end{pmatrix}, \quad (26)$$

where $A_{\mathbf{k}\mathbf{k}'}(\mathbf{r}) = \Psi^\dagger_{n+,\mathbf{k}}(\mathbf{r})\Psi_{n+,\mathbf{k}'}(\mathbf{r})$, $B_{\mathbf{k}\mathbf{k}'}(\mathbf{r}) = \Psi^\dagger_{n+,\mathbf{k}}(\mathbf{r})\Psi_{n-,\mathbf{k}'}(\mathbf{r})$, $C_{\mathbf{k}\mathbf{k}'}(\mathbf{r}) = \Psi^\dagger_{n-,\mathbf{k}}(\mathbf{r})\Psi_{n+,\mathbf{k}'}(\mathbf{r}) = B^*_{\mathbf{k}'\mathbf{k}}(\mathbf{r})$, and $D_{\mathbf{k}\mathbf{k}'}(\mathbf{r}) = \Psi^\dagger_{n-,\mathbf{k}}(\mathbf{r})\Psi_{n-,\mathbf{k}'}(\mathbf{r})$. The above matrix commutes with 1_4, $\tau_z 1_2$, $\tau_y\tilde{\sigma}_y$, and $\tau_x\tilde{\sigma}_y$ where the Pauli matrices τ act in the valley space and $\tilde{\sigma}$ in the $n\pm$ band space [30]. Together with the spin SU(2) generators, they form the 16 generators of the global spin-valley U(4) symmetry first pointed out by Bultinck *et al.* Ref. [21]. At this point, we have not used the $\mathcal{C}$ symmetry, only $C_2\mathcal{T}$ and P; therefore, this U(4) symmetry is present even away from the chiral limit, if we neglect the small angle rotation of the Pauli matrices in $\hat{H}_{BM}$ [Eq. (1)] [11]. We will adopt the nomenclature of Ref. [32] and refer to this as the nonchiral flat spin-valley U(4) symmetry.

The consequences of the $\mathcal{C}$ symmetry are more transparent in the Φ basis [Eq. (8)]. Expanding the fields as

$$\chi_\sigma(\mathbf{r}) = \begin{pmatrix}\psi_\sigma(\mathbf{r})\\ \phi_\sigma(\mathbf{r})\end{pmatrix} = \sum_{\mathbf{k}}\sum_{\lambda=\pm}\begin{pmatrix}\Phi_{\lambda,\mathbf{k}}(\mathbf{r})e_{\sigma,\mathbf{K},\lambda,\mathbf{k}}\\ e^{i\alpha^{\mathcal{C}}_{\mathbf{k}}}\Phi^*_{\lambda,\mathbf{k}}(\mathbf{r})e_{\sigma,\mathbf{K}',-\lambda,-\mathbf{k}-\mathbf{q}_1}\end{pmatrix}, \tag{27}$$

and using Eqs. (17)–(19), we find

$$\chi^\dagger_\sigma(\mathbf{r})\chi_\sigma(\mathbf{r}) = \sum_{\mathbf{k}\mathbf{k}'}(e^\dagger_{\sigma,\mathbf{K},+,\mathbf{k}}, e^\dagger_{\sigma,\mathbf{K},-,\mathbf{k}}, e^\dagger_{\sigma,\mathbf{K}',-,\mathbf{k}}, e^\dagger_{\sigma,\mathbf{K}',+,\mathbf{k}})\begin{pmatrix}\bar{A}_{\mathbf{k}\mathbf{k}'}(\mathbf{r}) & 0 & 0 & 0\\ 0 & \bar{D}_{\mathbf{k}\mathbf{k}'}(\mathbf{r}) & 0 & 0\\ 0 & 0 & \bar{D}_{\mathbf{k}\mathbf{k}'}(\mathbf{r}) & 0\\ 0 & 0 & 0 & \bar{A}_{\mathbf{k}\mathbf{k}'}(\mathbf{r})\end{pmatrix}\begin{pmatrix}e_{\sigma,\mathbf{K},+,\mathbf{k}'}\\ e_{\sigma,\mathbf{K},-,\mathbf{k}'}\\ e_{\sigma,\mathbf{K}',-,\mathbf{k}'}\\ e_{\sigma,\mathbf{K}',+,\mathbf{k}'}\end{pmatrix}, \tag{28}$$

where $\bar{A}_{\mathbf{k}\mathbf{k}'}(\mathbf{r}) = \Phi^\dagger_{+,\mathbf{k}}(\mathbf{r})\Phi_{+,\mathbf{k}'}(\mathbf{r})$ and $\bar{D}_{\mathbf{k}\mathbf{k}'}(\mathbf{r}) = \Phi^\dagger_{-,\mathbf{k}}(\mathbf{r})\Phi_{-,\mathbf{k}'}(\mathbf{r})$. Clearly, in this basis, we can perform a global spin-valley U(4) rotation in the Chern basis $(e_{\sigma,\mathbf{K},+,\mathbf{k}}, e_{\sigma,\mathbf{K}',+,\mathbf{k}})$ and an independent spin-valley U(4) rotation in the opposite Chern basis $(e_{\sigma,\mathbf{K},-,\mathbf{k}}, e_{\sigma,\mathbf{K}',-,\mathbf{k}})$, leading to the spin valley U(4)× U(4) symmetry in the chiral limit first pointed out by Bultinck *et al.* [21] (see, also, Refs. [30,32]). Adopting the nomenclature of Ref. [32], we will refer to this as the (first) chiral-flat U(4) × U(4) symmetry.

In Appendix B, we relate the generators of the nonchiral flat U(4) to the generators of the (first) chiral flat U(4) × U(4) (as was also done in Refs. [21,32]). Performing an arbitrary nonchiral flat U(4) global rotation is equivalent to rotating the Chern basis $(e_{\sigma,\mathbf{K},+,\mathbf{k}}, e_{\sigma,\mathbf{K}',+,\mathbf{k}})$ by $\exp[i(\omega_0\tau_0 + \omega_z\tau_z + \omega_1\tau_x + \omega_2\tau_y)]$ while simultaneously rotating the opposite Chern basis $(e_{\sigma,\mathbf{K},-,\mathbf{k}}, e_{\sigma,\mathbf{K}',-,\mathbf{k}})$ by $\exp[i(\omega_0\tau_0 + \omega_z\tau_z - \omega_1\tau_x - \omega_2\tau_y)]$. This can be thought of as a mirror reflecting an axial vector $\vec{\omega}$ about the xy plane.

Note that if $\delta\rho(\mathbf{r})$ acts on the $\nu = 0$ fully valley polarized state, such as $|\Omega_{\nu=0}\rangle = \prod_{\mathbf{k},n=\pm} d^\dagger_{\uparrow,\mathbf{K},n,\mathbf{k}} d^\dagger_{\downarrow,\mathbf{K},n,\mathbf{k}}|0\rangle$, then $\delta\rho(\mathbf{r})$ annihilates it. Because H_{int} is positive semidefinite, this is therefore a ground state of H_{int}. Due to the U(4) × U(4) symmetry, any state obtained by such global rotation is also annihilated and is therefore degenerate with the valley polarized state. Using P [Eq. (19)], $C_2\mathcal{T}$ [Eq. (18)], and Eq. (8), we have

$$\sum_{\mathbf{k}}\sum_{n=\pm}\Psi^\dagger_{n,\mathbf{k}}(\mathbf{r})\Psi_{n,\mathbf{k}}(\mathbf{r}) = 2\sum_{\mathbf{k}}\Phi^\dagger_{+,\mathbf{k}}(\mathbf{r})\Phi_{+,\mathbf{k}}(\mathbf{r}) \tag{29}$$

$$= 2\sum_{\mathbf{k}}\Phi^\dagger_{-,\mathbf{k}}(\mathbf{r})\Phi_{-,\mathbf{k}}(\mathbf{r}). \tag{30}$$

Therefore, for any integer filled Chern state $|\Omega_\nu\rangle$, we have

$$\delta\rho(\mathbf{r})|\Omega_\nu\rangle = \delta\bar{\rho}_\nu(\mathbf{r})|\Omega_\nu\rangle, \tag{31}$$

$$\delta\bar{\rho}_\nu(\mathbf{r}) = \nu\sum_{\mathbf{k}}\Phi^\dagger_{+,\mathbf{k}}(\mathbf{r})\Phi_{+,\mathbf{k}}(\mathbf{r}) = \nu\sum_{\mathbf{k}}\Phi^\dagger_{-,\mathbf{k}}(\mathbf{r})\Phi_{-,\mathbf{k}}(\mathbf{r})$$
$$= \frac{\nu}{2}\sum_{\mathbf{k}}\sum_{n=\pm}\Psi^\dagger_{n,\mathbf{k}}(\mathbf{r})\Psi_{n,\mathbf{k}}(\mathbf{r}). \tag{32}$$

The last equality will be useful when we switch to the 2D exponentially localized Wannier basis because it corresponds to the sum over all states of the two narrow bands whose total Chern number vanishes, for which the localized basis can always be found [7].

A. Excitations in the strong coupling

In the strong coupling, the energy of an operator X acting on the Chern state $|\Omega_\nu\rangle$ at integer filling ν can be obtained as

$$EX|\Omega_\nu\rangle = H_{\text{int}}X|\Omega_\nu\rangle. \tag{33}$$

Substituting (22) and using (31), we readily find

$$\left(E - E^{(0)}_\nu\right)X|\Omega_\nu\rangle$$
$$= \frac{1}{2}\int d^2\mathbf{r}d^2\mathbf{r}'V(\mathbf{r}-\mathbf{r}')[\delta\rho(\mathbf{r}),[\delta\rho(\mathbf{r}'),X]]|\Omega_\nu\rangle$$
$$+ \int d^2\mathbf{r}d^2\mathbf{r}'V(\mathbf{r}-\mathbf{r}')[\delta\rho(\mathbf{r}),X]\delta\bar{\rho}_\nu(\mathbf{r}')|\Omega_\nu\rangle, \tag{34}$$

where $E^{(0)}_\nu = \frac{1}{2}\int d^2\mathbf{r}d^2\mathbf{r}'V(\mathbf{r}-\mathbf{r}')\delta\bar{\rho}_\nu(\mathbf{r})\delta\bar{\rho}_\nu(\mathbf{r}')$ is a real number, and $\delta\bar{\rho}_\nu(\mathbf{r})$ was defined in Eq. (32). The key observation is that the commutators on the right-hand side of Eq. (34) do not change the number of creation and annihilation operators in X because $\delta\rho(\mathbf{r})$, defined in Eq. (23), is a charge neutral bilinear. Therefore, we can just match the operator coefficients on each side of the equation to find their spectra (assuming again that X does not annihilate $|\Omega_\nu\rangle$, in which case it is trivial).

B. Single particle excitation using Bloch basis

To facilitate the calculation, we note that if we rearrange the components as

$$\mathfrak{d}_{\mathbf{k}} = \begin{pmatrix}d_{\sigma,\mathbf{K},+,\mathbf{k}}\\ d_{\sigma,\mathbf{K},-,\mathbf{k}}\\ d_{\sigma,\mathbf{K}',-,\mathbf{k}}\\ -d_{\sigma,\mathbf{K}',+,\mathbf{k}}\end{pmatrix}, \tag{35}$$

then we can write the projected density in Eq. (26) as

$$\chi^\dagger_\sigma(\mathbf{r})\chi_\sigma(\mathbf{r}) = \sum_{\mathbf{k}\mathbf{k}'}\mathfrak{d}^\dagger_{n,\mathbf{k},\sigma,\kappa}\Psi^\dagger_{n,\mathbf{k}}(\mathbf{r})\Psi_{n',\mathbf{k}'}(\mathbf{r})\mathfrak{d}_{n',\mathbf{k}',\sigma,\kappa}, \tag{36}$$

where repeated subscripts are summed. The above expression is explicitly U(4) symmetric.

To compute the energy spectrum of a single hole added to the strong coupling ground state, we let $X = \mathfrak{d}_{n,\mathbf{k},\sigma,\kappa}$. For a single electron, we let $X = \mathfrak{d}^\dagger_{n,\mathbf{k},\sigma,\kappa}$. Such spectra were presented in Refs. [30,31]. In addition, spectra for the charge neutral (excitonic) excitation were computed in Refs. [30,31,40] and for the charge ± 2 excitations in Ref. [31]. We note in passing that in order to determine the degeneracy, we also need to consider the nature of the ground state to make sure X does not annihilate it.

Substituting into Eq. (34), and using the discrete translational invariance of the moiré lattice, we find

$$\begin{aligned}\left(E - E_\nu^{(0)}\right)\mathfrak{d}_{n,\mathbf{k},\sigma,\kappa}|\Omega_\nu\rangle &= \frac{1}{2}\int d^2\mathbf{r}d^2\mathbf{r}' V(\mathbf{r}-\mathbf{r}')\sum_m\sum_{m'\mathbf{p}'}\Psi^\dagger_{n,\mathbf{k}}(\mathbf{r}')\Psi_{m',\mathbf{p}'}(\mathbf{r}')\Psi^\dagger_{m',\mathbf{p}'}(\mathbf{r})\Psi_{m,\mathbf{k}}(\mathbf{r})\mathfrak{d}_{m,\mathbf{k},\sigma,\kappa}|\Omega_\nu\rangle \\ &\quad - \frac{\nu}{2}\int d^2\mathbf{r}d^2\mathbf{r}' V(\mathbf{r}-\mathbf{r}')\sum_{m'\mathbf{p}'}\sum_m\Psi^\dagger_{m',\mathbf{p}'}(\mathbf{r}')\Psi_{m',\mathbf{p}'}(\mathbf{r}')\Psi^\dagger_{n,\mathbf{k}}(\mathbf{r})\Psi_{m,\mathbf{k}}(\mathbf{r})\mathfrak{d}_{m,\mathbf{k},\sigma,\kappa}|\Omega_\nu\rangle, \qquad (37)\\ \left(E - E_\nu^{(0)}\right)\mathfrak{d}^\dagger_{n,\mathbf{k},\sigma,\kappa}|\Omega_\nu\rangle &= \frac{1}{2}\int d^2\mathbf{r}d^2\mathbf{r}' V(\mathbf{r}-\mathbf{r}')\sum_m\sum_{m'\mathbf{p}'}\Psi^\dagger_{m',\mathbf{p}'}(\mathbf{r}')\Psi_{n,\mathbf{k}}(\mathbf{r}')\Psi^\dagger_{m,\mathbf{k}}(\mathbf{r})\Psi_{m',\mathbf{p}'}(\mathbf{r})\mathfrak{d}^\dagger_{m,\mathbf{k},\sigma,\kappa}|\Omega_\nu\rangle \\ &\quad + \frac{\nu}{2}\int d^2\mathbf{r}d^2\mathbf{r}' V(\mathbf{r}-\mathbf{r}')\sum_{m'\mathbf{p}'}\sum_m\Psi^\dagger_{m',\mathbf{p}'}(\mathbf{r}')\Psi_{m',\mathbf{p}'}(\mathbf{r}')\Psi^\dagger_{m,\mathbf{k}}(\mathbf{r})\Psi_{n,\mathbf{k}}(\mathbf{r})\mathfrak{d}^\dagger_{m,\mathbf{k},\sigma,\kappa}|\Omega_\nu\rangle. \qquad (38)\end{aligned}$$

We see that the right-hand side is a linear combination of operators $\mathfrak{d}_{n,\mathbf{k},\sigma,\kappa}$ on the left-hand side, which means that the above equation can be satisfied if we perform an appropriate unitary transformation on the operators on both sides. Because the momentum $\mathbf{k}$ of the operators on both sides is the same, as are the spin σ and valley κ, to find the energy spectrum of the single particle excitations, we just need to diagonalize a 2×2 matrix in the band indices n, m. The matrix is Hermitian due to the interaction potential $V(\mathbf{r}-\mathbf{r}')$ being even under particle exchange, which, together with $C_2\mathcal{T}$ [Eq. (6)], allows us to show that this matrix differs for the hole and the particle only by the direct (Hartree) term,

$$\begin{aligned}\mathcal{H}^{h/p}_{nm}(\mathbf{k}) &= \frac{1}{2}\int d^2\mathbf{r}d^2\mathbf{r}' V(\mathbf{r}-\mathbf{r}')\sum_{m'\mathbf{p}'}\Psi^\dagger_{n,\mathbf{k}}(\mathbf{r})\Psi_{m',\mathbf{p}'}(\mathbf{r})\Psi^\dagger_{m',\mathbf{p}'}(\mathbf{r}')\Psi_{m,\mathbf{k}}(\mathbf{r}') \\ &\quad \mp \frac{\nu}{2}\int d^2\mathbf{r}d^2\mathbf{r}' V(\mathbf{r}-\mathbf{r}')\sum_{m'\mathbf{p}'}\Psi^\dagger_{m',\mathbf{p}'}(\mathbf{r})\Psi_{m',\mathbf{p}'}(\mathbf{r})\Psi^\dagger_{n,\mathbf{k}}(\mathbf{r}')\Psi_{m,\mathbf{k}}(\mathbf{r}'). \qquad (39)\end{aligned}$$

The matrix $\mathcal{H}^{h/p}_{nm}(\mathbf{k})$ is diagonal in nm for each $\mathbf{k}$. This is because, according to Eq. (6), each $\Psi_{n,\mathbf{k}}(\mathbf{r})$ is a $C_2\mathcal{T}$ eigenstate with an eigenvalue $+1$, and because we can use $\mathcal{C}$ to flip between the signs of n utilizing Eq. (9). Moreover, $C_2\mathcal{T} = 1_2\sigma_x\mathcal{K}$, while $\mathcal{C} = 1_2\sigma_z$. Therefore, $\mathcal{C}C_2\mathcal{T} = i1_2\sigma_y\mathcal{K}$ squares to -1. It is clearly antiunitary and does not change $\mathbf{k}$. Therefore, at any $\mathbf{k}$, $\mathcal{C}C_2\mathcal{T}$ guarantees that

$$\begin{pmatrix}0 & 1\\ -1 & 0\end{pmatrix}_{nn'}\mathcal{H}^{*h/p}_{n'm'}(\mathbf{k})\begin{pmatrix}0 & -1\\ 1 & 0\end{pmatrix}_{m'm} = \mathcal{H}^{h/p}_{nm}(\mathbf{k}). \qquad (40)$$

Because it is a Hermitian 2×2 matrix, the above guarantees that $\mathcal{H}^{h/p}_{nm}(\mathbf{k})$ is proportional to the identity matrix 1_2 in the chiral limit, i.e., the two eigenvalues are degenerate at each $\mathbf{k}$. The contribution from the first (exchange) and the second (direct, divided by $\mp\nu$) lines in Eq. (39) are shown in Fig. 2. To obtain the actual degeneracies of the bands, we need to consider whether acting with a particular linear combination of d's or $d^\dagger$'s annihilates the ground state [which, up to the U(4) $\times$ U(4) transformation, is a product state of the Chern states]. For example, for $\nu = 1$, there are three ways to add a (light) particle and five ways to add a (heavy) hole [34]. For a general non-negative integer filling $\nu \geqslant 0$, the particle branch is $(4-\nu)$-fold degenerate (because there are $4-\nu$ ways to add a particle without annihilating the many-body product state) and the hole branch is $(4+\nu)$-fold degenerate (because there are $4+\nu$ ways to add a hole). The degeneracies for negative integer filling $\nu < 0$ are related by the particle-hole transformation: the hole branch is $(4-|\nu|)$-fold degenerate and the particle branch is $(4+|\nu|)$-fold degenerate.

Away from the chiral limit, $\mathcal{C}$ is no longer exact. However, to a good approximation [16], even away from the chiral limit we still have P. Because $PC_2\mathcal{T}$ is also antiunitary and squares to -1, and because it changes $\mathbf{k}$ to $-\mathbf{k}-\mathbf{q}_1$, $\mathcal{H}^{h/p}_{nm}(\mathbf{k})$ must be diagonal at all momenta left invariant under P, namely, $\boldsymbol{\Gamma}$ and $\boldsymbol{M}$. Away from these $\mathbf{k}$ points, the spectrum is split, as shown in Refs. [30,31,34]. For a range of angles near the magic, evaluating the spectrum in the Bloch basis requires numerical determination of the wave functions $\Psi_{n,\mathbf{k}}(\mathbf{r})$, although exactly at the magic angle and the chiral limit, one should only need the numerical determination of the wave functions at $\mathbf{K}_m$ [17]. Nevertheless, the reason for the shape of the spectrum thus obtained is somewhat obscured in the Bloch basis. To better reveal its character, we now switch to the Wannier basis.

IV. WANNIER STATES IN THE CHIRAL LIMIT

We now turn to the main part of the paper, where we use the projection method [33] to construct the exponentially localized Wannier states in the chiral limit. There are two Wannier states per unit cell in the valley $\mathbf{K}$, namely, $w_{\mathbf{R},j}(\mathbf{r})$ with $j = 1 \equiv AB$ and $j = 2 \equiv BA$. For a fixed triangular moiré

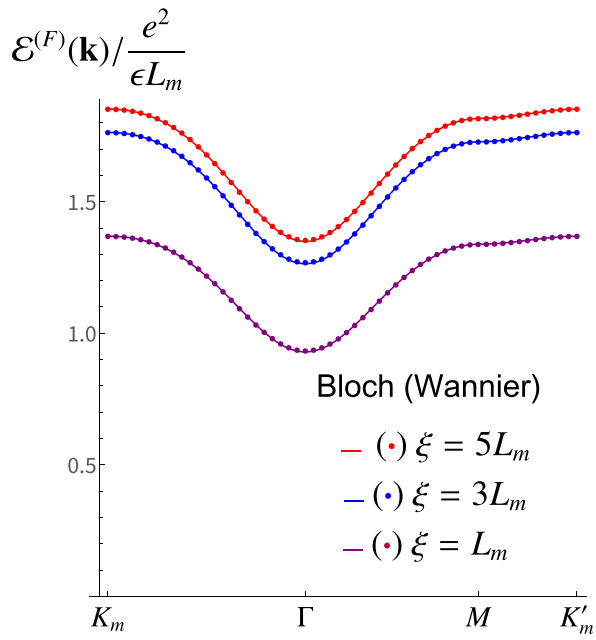

(a)

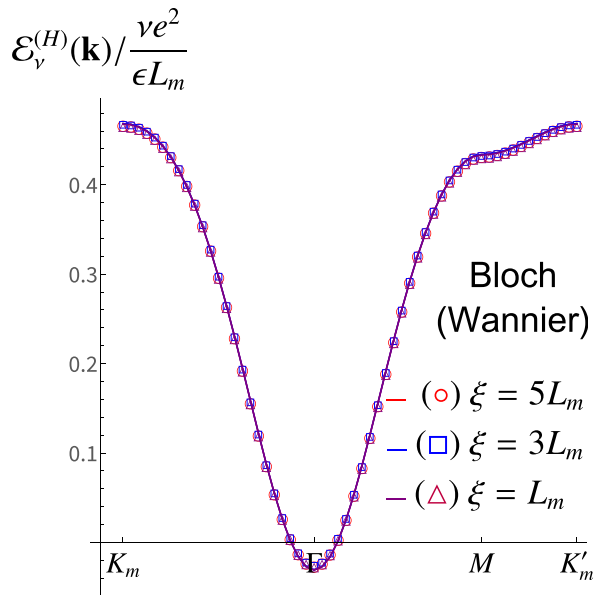

(b)

FIG. 2. (a) The exchange and (b) the direct contributions to the single particle dispersion in the strong coupling limit along the high symmetry path shown in Fig. 1(b) for different values of ξ, the distance between the TBG and the metallic gates. L_m is the period of the triangular moiré lattice and the energy is expressed in Coulomb units, $e^2/(\epsilon L_m)$. The solid colored curves are given by Eq. (39) using Bloch states. The dots and other symbols denote the dispersion obtained from the Wannier based tight-binding model on a triangular lattice with hopping distances no longer than $2L_m$ [Eqs. (63), (68), and (69)]. Note that unlike the exchange contribution, the direct contribution in (b) is almost independent of ξ for $\xi \gtrsim L_m$.

lattice vector $\mathbf{R} = m_1\mathbf{L}_1 + m_2\mathbf{L}_2$ with integer $m_{1,2}$, they are distinguished by the position of their center on the dual honeycomb lattice which is either *AB* or *BA* [see Fig. 1(a)]. The exponentially localized Wannier states can be obtained from the Fourier transform of an appropriate linear combination of the Bloch states $\Phi_{\pm,\mathbf{k}}$ distinguished by their sublattice polarization (8) as

$$w_{\mathbf{R},j}(\mathbf{r}) = \frac{1}{\sqrt{N_{uc}}}\sum_{\mathbf{k}} e^{-i\mathbf{k}\cdot\mathbf{R}}\tilde{\Phi}_{j,\mathbf{k}}(\mathbf{r}), \tag{41}$$

$$\tilde{\Phi}_{j,\mathbf{k}}(\mathbf{r}) = \sum_{m=\pm}\Phi_{m,\mathbf{k}}(\mathbf{r})\mathcal{U}_{mj}(\mathbf{k}), \tag{42}$$

$$\mathcal{U}_{mj}(\mathbf{k}) = \mathrm{UP}\left[\int d^2\mathbf{r}\Phi^\dagger_{m,\mathbf{k}}(\mathbf{r})h_j(\mathbf{r})\right]. \tag{43}$$

In the above, UP stands for "unitary part" and $h_j(\mathbf{r})$ are the trial functions (at each valley there are two trial functions; the trial functions at valley $\mathbf{K}'$ are related to the trial functions at $\mathbf{K}$ by spinless time reversal symmetry, i.e., complex conjugation). The most practical method for constructing the UP of the $\mathbf{k}$-dependent 2×2 matrix,

$$A_{mj}(\mathbf{k}) = \int d^2\mathbf{r}\Phi^\dagger_{m,\mathbf{k}}(\mathbf{r})h_j(\mathbf{r}), \tag{44}$$

is via singular value decomposition (SVD), and replacing the diagonal part of the SVD with an identity matrix [33]. This procedure is justified provided none of the singular values of $A_{mj}(\mathbf{k})$ vanish at some $\mathbf{k}$; otherwise, there would be an obstruction to the exponential localization of Wannier states [33].

A particularly appealing choice for the trial functions in the chiral limit $w_0/w_1 = 0$ is

$$h_1(\mathbf{r}) = \begin{pmatrix} i \\ 0 \\ 0 \\ -\varepsilon^* \end{pmatrix}\delta(\mathbf{r}-\mathbf{r}_{AB}), \tag{45}$$

$$h_2(\mathbf{r}) = \varepsilon^* C_2'\mathcal{T}h_1(\mathbf{r}) = \begin{pmatrix} 0 \\ -1 \\ -i\varepsilon^* \\ 0 \end{pmatrix}\delta(\mathbf{r}-\mathbf{r}_{BA}), \tag{46}$$

where $\mathbf{r}_{AB} = \frac{1}{3}(\mathbf{L}_1+\mathbf{L}_2)$, $\mathbf{r}_{BA} = \frac{1}{3}(2\mathbf{L}_2-\mathbf{L}_1)$, $\varepsilon = e^{2\pi i/3} = e^{-i\mathbf{q}_1\cdot\mathbf{r}_{AB}} = e^{-i\mathbf{q}_1\cdot\mathbf{r}_{BA}}$, and $\delta(\mathbf{r})$ is the 2D Dirac δ function. With this choice, the singular values of $A_{mj}(\mathbf{k})$ are degenerate, never vanish, and are relatively weakly $\mathbf{k}$ dependent (see Fig. 3). This immediately implies that the Wannier states are 2D exponentially localized.

Moreover, not only do we guarantee the on-site representation of $C_2'\mathcal{T}$—which is incorporated by construction—but, remarkably, we simultaneously obtain simple representation of P, $\mathcal{C}C_2\mathcal{T}$, and C_3. We demonstrate this in Appendix A. The $C_2\mathcal{T}$ alone remains obstructed and cannot be represented on-site.

Action of the symmetries on the Wannier states

As detailed in Appendix A, the action of the particle-hole symmetry (10) on the Wannier states (41) is

$$P: \quad -i\mu_y 1_2 w_{\mathbf{R},1}(-\mathbf{r}) = -\varepsilon^* e^{i\mathbf{q}_1\cdot\mathbf{R}} w_{-\mathbf{R}-\mathbf{L}_2,2}(\mathbf{r}), \tag{47}$$

$$-i\mu_y 1_2 w_{\mathbf{R},2}(-\mathbf{r}) = \varepsilon^* e^{i\mathbf{q}_1\cdot\mathbf{R}} w_{-\mathbf{R}-\mathbf{L}_2,1}(\mathbf{r}). \tag{48}$$

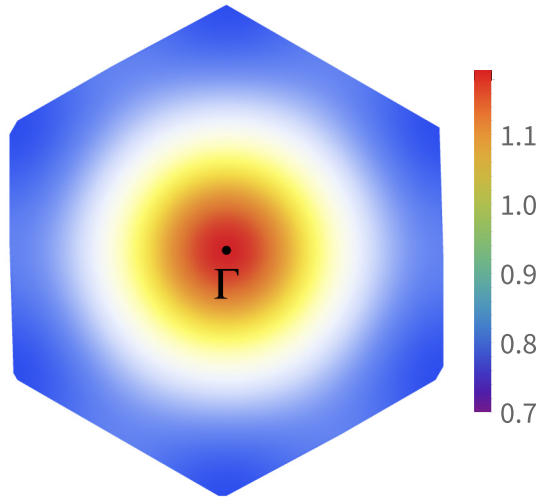

FIG. 3. The (degenerate) singular values of the matrix $A_{mj}(\mathbf{k})$ defined in Eq. (44) with the trial functions in Eqs. (45) and (46).

Similarly, we derive the action of $C_2\mathcal{T}$ followed by $\mathcal{C}$ in Appendix A to be

$$\mathcal{C}C_2\mathcal{T}: \quad i1_2\sigma_y w^*_{\mathbf{R},1}(-\mathbf{r}) = -iw_{-\mathbf{R}-\mathbf{L}_2,2}(\mathbf{r}), \tag{49}$$

$$i1_2\sigma_y w^*_{\mathbf{R},2}(-\mathbf{r}) = iw_{-\mathbf{R}-\mathbf{L}_2,1}(\mathbf{r}). \tag{50}$$

Time reversal followed by the in-plane twofold rotation along the y axis gives

$$C_2'\mathcal{T}: \quad \mu_x 1_2 w^*_{\mathbf{R},1}(-x,y) = \varepsilon w_{-R_x,R_y,2}(x,y), \tag{51}$$

$$\mu_x 1_2 w^*_{\mathbf{R},2}(-x,y) = \varepsilon w_{-R_x,R_y,1}(x,y), \tag{52}$$

which follows using the similar arguments detailed in the Appendix and the definition of h_2 via the action of $C_2'\mathcal{T}$ on h_1 in Eq. (46). Finally, the action of threefold rotations about the axis perpendicular to the plane on the Wannier states gives

$$\begin{aligned} C_3: e^{-i\frac{\pi}{3}1_2\sigma_z}e^{-i\frac{2\pi}{3}\hat{\ell}_z}w_{\mathbf{R},1}(\mathbf{r}) \\ = e^{-i\frac{\pi}{3}}w_{(-\frac{1}{2}R_x-\frac{\sqrt{3}}{2}R_y,-\frac{1}{2}R_y+\frac{\sqrt{3}}{2}R_x)-\mathbf{L}_1,1}(\mathbf{r}), \end{aligned} \tag{53}$$

$$\begin{aligned} e^{-i\frac{\pi}{3}1_2\sigma_z}e^{-i\frac{2\pi}{3}\hat{\ell}_z}w_{\mathbf{R},2}(\mathbf{r}) \\ = e^{i\frac{\pi}{3}}w_{(-\frac{1}{2}R_x-\frac{\sqrt{3}}{2}R_y,-\frac{1}{2}R_y+\frac{\sqrt{3}}{2}R_x)-\mathbf{L}_2,2}(\mathbf{r}). \end{aligned} \tag{54}$$

Combining P and $\mathcal{C}C_2\mathcal{T}$, we have an unobstructed symmetry [16] and

$$w_{\mathbf{R},j}(\mathbf{r}) = i\mu_y\sigma_y\varepsilon^* e^{i\mathbf{q}_1\cdot\mathbf{R}}w^*_{\mathbf{R},j}(\mathbf{r}). \tag{55}$$

Therefore, if we let

$$\tilde{}_{\mathbf{R},j}(\mathbf{r}) = e^{i\frac{\pi}{12}}e^{-\frac{i}{2}\mathbf{q}_1\cdot\mathbf{R}}w_{\mathbf{R},j}(\mathbf{r}), \tag{56}$$

then

$$\tilde{w}_{\mathbf{R},j}(\mathbf{r}) = \mu_y\sigma_y\tilde{w}^*_{\mathbf{R},j}(\mathbf{r}), \tag{57}$$

and we therefore reach an important conclusion, namely,

$$\tilde{w}^\dagger_{\mathbf{R},j}(\mathbf{r})\tilde{w}_{\mathbf{R}',j'}(\mathbf{r}) \in \text{Reals}. \tag{58}$$

This is because expanding the fields in the $\tilde{w}$ basis,

$$\chi_\sigma(\mathbf{r}) = \sum_{\mathbf{R}}\sum_{j=1,2}\begin{pmatrix}\tilde{w}_{\mathbf{R},j}(\mathbf{r})f_{\sigma,\mathbf{K},j,\mathbf{R}} \\ \tilde{w}^*_{\mathbf{R},j}(\mathbf{r})f_{\sigma,\mathbf{K}',j,\mathbf{R}}\end{pmatrix}, \tag{59}$$

then gives the projected density operator,

$$\begin{aligned} \chi^\dagger_\sigma(\mathbf{r})\chi_\sigma(\mathbf{r}) = \sum_{\mathbf{R},\mathbf{R}'}\sum_{j,j'}\tilde{w}^\dagger_{\mathbf{R},j}(\mathbf{r})\tilde{w}_{\mathbf{R}',j'}(\mathbf{r}) \\ \times(f^\dagger_{\sigma,\mathbf{K},j,\mathbf{R}}f_{\sigma,\mathbf{K},j',\mathbf{R}'} + f^\dagger_{\sigma,\mathbf{K}',j,\mathbf{R}}f_{\sigma,\mathbf{K}',j',\mathbf{R}'}), \end{aligned} \tag{60}$$

which is explicitly invariant under a spin-valley U(4) rotation. Here, the fermion operator $f_{\sigma,\kappa,j,\mathbf{R}}$ annihilates the Wannier state at site $\mathbf{R}$, sublattice j, spin σ, and valley $\kappa = \mathbf{K}, \mathbf{K}'$. In Appendix B, we relate this U(4) subgroup, dubbed chiral nonflat U(4) in Ref. [32], to the (first) chiral-flat limit U(4) × U(4) symmetry. Performing an arbitrary chiral nonflat U(4) global rotation is equivalent to simultaneously rotating the aforementioned Chern bases $(e_{\sigma,\mathbf{K},+,\mathbf{k}}, e_{\sigma,\mathbf{K}',+,\mathbf{k}})$ and $(e_{\sigma,\mathbf{K},-,\mathbf{k}}, e_{\sigma,\mathbf{K}',-,\mathbf{k}})$ by the *same* transformation, say, $\exp[i(\omega_0\tau_0 + \omega_z\tau_z + \omega_1\tau_x + \omega_2\tau_y)]$. This is unlike in the nonchiral flat U(4), where the axial vector $\vec{\omega}$ was reflected about the xy plane.

Because these overlaps in Eq. (58) will be used in determining the form of the projected interactions, it will be helpful to visualize them. This is done in Fig. 4.

Finally, note that the exactly flat band dispersion of the kinetic energy at the magic angle of the chiral limit is trivially satisfied because the action of the kinetic energy operator on the Wannier states annihilates them.

V. SINGLE PARTICLE EXCITATIONS IN THE STRONG COUPLING IN THE WANNIER STATE BASIS

In order to rewrite $\mathcal{H}^{h/p}(\mathbf{k})$ in the Wannier basis, we first note that

$$\mathcal{F}(\mathbf{r},\mathbf{r}') \equiv \sum_{m\mathbf{p}}\Psi_{m,\mathbf{p}}(\mathbf{r})\Psi^\dagger_{m,\mathbf{p}}(\mathbf{r}') \tag{61}$$

$$= \sum_{m\mathbf{p}}\tilde{\Phi}_{j,\mathbf{p}}(\mathbf{r})\tilde{\Phi}^\dagger_{j,\mathbf{p}}(\mathbf{r}') = \sum_{j,\mathbf{R}}w_{\mathbf{R},j}(\mathbf{r})w^\dagger_{\mathbf{R},j}(\mathbf{r}') \tag{62}$$

where in the first line we used the fact that the transformation from $\Psi_{m,\mathbf{p}}(\mathbf{r})$ to $\tilde{\Phi}_{j,\mathbf{p}}(\mathbf{r})$ is unitary (as, of course, is the final transformation to w's).

Using the same sequence of unitary transformations, we can then rewrite Eq. (39) in the Wannier basis as

$$\mathcal{H}^{h/p}_{nm}(\mathbf{k}) \to \tilde{\mathcal{H}}^{h/p}_{jj'}(\mathbf{k}) = \mathcal{E}^{(F)}_{jj'}(\mathbf{k}) + \mathcal{E}^{(H)}_{\nu,jj'}(\mathbf{k}), \tag{63}$$

$$\begin{aligned} \mathcal{E}^{(F)}_{jj'}(\mathbf{k}) = \frac{1}{2N_{uc}}\sum_{\mathbf{R}\mathbf{R}'}e^{-i\mathbf{k}\cdot(\mathbf{R}-\mathbf{R}')}\int d^2\mathbf{r}d^2\mathbf{r}' \\ \times V(\mathbf{r}-\mathbf{r}')w^\dagger_{\mathbf{R},j}(\mathbf{r})\mathcal{F}(\mathbf{r},\mathbf{r}')w_{\mathbf{R}',j'}(\mathbf{r}'), \end{aligned} \tag{64}$$

$$\begin{aligned} \mathcal{E}^{(H)}_{\nu,jj'}(\mathbf{k}) = \mp\frac{\nu}{2N_{uc}}\sum_{\mathbf{R}\mathbf{R}'}e^{-i\mathbf{k}\cdot(\mathbf{R}-\mathbf{R}')}\int d^2\mathbf{r}d^2\mathbf{r}' \\ \times V(\mathbf{r}-\mathbf{r}')w^\dagger_{\mathbf{R},j}(\mathbf{r}')w_{\mathbf{R}',j'}(\mathbf{r}')\mathrm{Tr}\mathcal{F}(\mathbf{r},\mathbf{r}). \end{aligned} \tag{65}$$

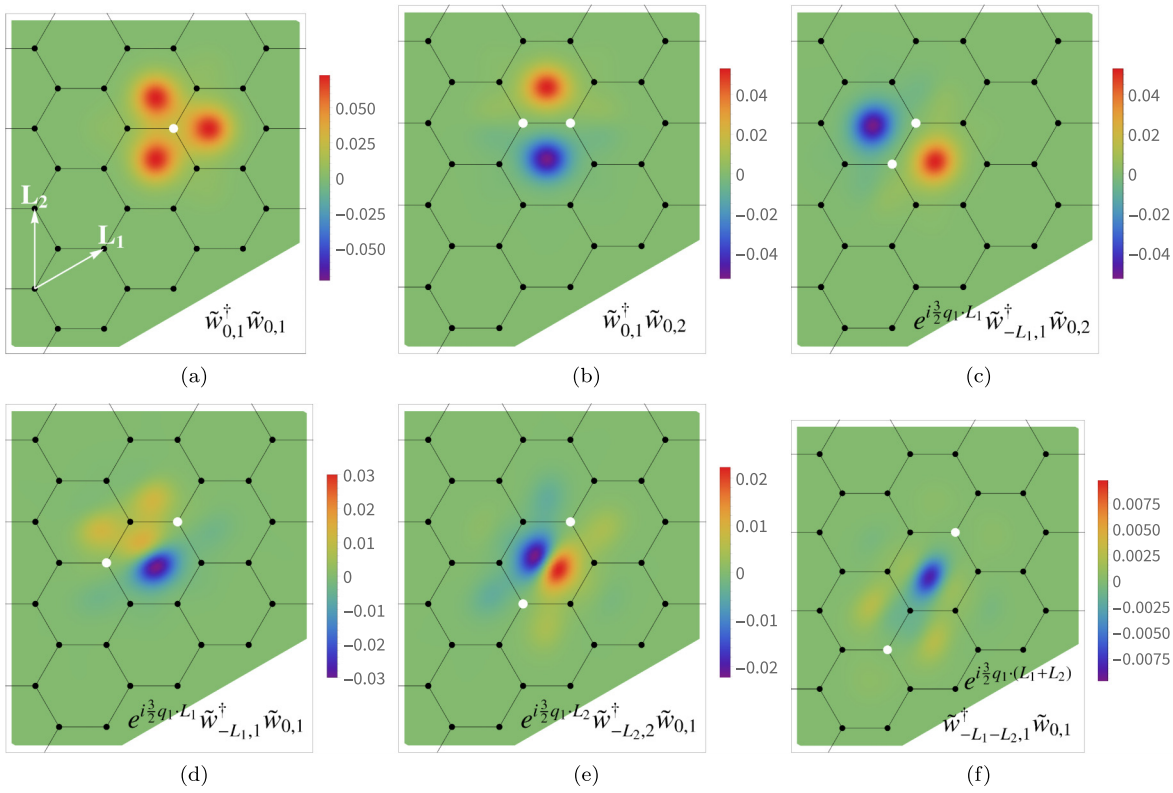

FIG. 4. The real-space plot of the combination of the Wannier orbitals entering into Eqs. (72) and (73), $e^{-i\frac{3}{2}\mathbf{q}_1\cdot\mathbf{R}}\tilde{w}^{\dagger}_{\mathbf{R},j}(\mathbf{r})\tilde{w}_{\mathbf{R}',j'}(\mathbf{r})$, where $\tilde{w}_{\mathbf{R},j}(\mathbf{r})$ is related to $w_{\mathbf{R},j}(\mathbf{r})$ in Eq. (56). As shown in Sec. IV A, $\mathcal{PC}C_2T$ symmetry guarantees that these overlap functions are purely real. The Wannier centers, determined by $\mathbf{R}$ and j, are illustrated by the white dots; (a) the familiar three peak "fidget spinner" structure for on-site overlap (i.e., $\mathbf{R}=\mathbf{R}'$ and $j=j'$). As shown in (d), the overlap for the nearest neighbors on the triangular lattice is predominantly negative near the *AA* sites. As illustrated in Fig. 7(a), the on-site tight-binding parameter $t^{(F)}_{\mathbf{0}}$ is dominated by the electrostatic self-interaction of a "monopole" (a) and self-interaction of each of the "dipoles" (b),(c); it is clearly positive. The nearest-neighbor hopping parameter $t^{(F)}_{\mathbf{L}_1}$ is dominated by two terms: the electrostatic interaction between the (a) monopole and the (d) dipole, as well as the electrostatic interaction between the (b) dipole and the (c) dipole. It is obvious that both of these terms will lead to the negative $t^{(F)}_{\mathbf{L}_1}$.

where $\mathcal{F}(\mathbf{r},\mathbf{r}')$ was defined in (61). The indices j and j' now label the two sublattices of the moiré honeycomb lattice at which the Wannier states are centered.

We will now show that $\tilde{\mathcal{H}}^{h/p}_{jj'}(\mathbf{k})$ is also proportional to $\delta_{jj'}$ in the chiral limit. $\mathcal{C}C_2\mathcal{T}$ guarantees that

$$1_2\sigma_y w^{*}_{\mathbf{R},j}(-\mathbf{r}) = (-i\lambda_y)_{jj'} w_{-\mathbf{R}-\mathbf{L}_2,j'}(\mathbf{r}), \tag{66}$$

where $\lambda_y = \left(\begin{smallmatrix}0 & -i\\ i & 0\end{smallmatrix}\right)$. In addition, $\mathcal{F}(\mathbf{r},\mathbf{r}') = 1_2\sigma_y\mathcal{F}^{*}(-\mathbf{r},-\mathbf{r}')1_2\sigma_y$. Using these relations and $V(\mathbf{r}) = V(-\mathbf{r})$, we find that

$$\tilde{\mathcal{H}}^{h/p}_{jj'}(\mathbf{k}) = (\lambda_y)_{j\ell}\tilde{\mathcal{H}}^{*h/p}_{\ell\ell'}(\mathbf{k})(\lambda_y)_{\ell' j''}. \tag{67}$$

This means that the 2×2 matrix $\tilde{\mathcal{H}}^{h/p}_{jj'}(\mathbf{k})$ must be proportional to $\delta_{jj'}$ for each $\mathbf{k}$. Therefore, despite the Wannier centers coinciding with the *AB* and *BA* sites forming the moiré honeycomb lattice, the spectrum of $\tilde{\mathcal{H}}^{h/p}_{jj'}(\mathbf{k})$ and therefore of $\mathcal{H}^{h/p}(\mathbf{k})$ can be understood as originating from the hopping on the *triangular* moiré lattice. In other words, the hopping occurs on the *AB* triangular sublattice of the honeycomb moiré lattice independently of the hopping on the *BA* triangular sublattice. Because the Wannier states are exponentially localized, the expansion in the range of the hopping is expected to converge fast.

Using (41), we find that $\mathcal{E}^{(F)}_{jj'}(\mathbf{k})$ gives a triangular lattice hopping model with the hopping constants which indeed decay rapidly with distance. We can thus write $\mathcal{E}^{(F)}_{jj'}(\mathbf{k}) = \delta_{jj'}\mathcal{E}^{(F)}(\mathbf{k})$, where

$$\mathcal{E}^{(F)}(\mathbf{k}) = \sum_{\mathbf{R}} t^{(F)}_{\mathbf{R}} e^{i(\mathbf{k}-\mathbf{q}_1)\cdot\mathbf{R}}. \tag{68}$$

The result for the hopping amplitudes $t^{(F)}_{\mathbf{R}}$ for the Coulomb interaction is shown in Fig. 5(a), using the central site as the reference. Because the nearest-neighbor hopping constant is negative (and because the hopping amplitudes decay rapidly with distance), the minimum of the dispersion is at the $\mathbf{\Gamma}$ point.

For the second (direct) term in (63), we similarly have $\mathcal{E}^{(H)}_{\nu,jj'} = \mp\delta_{jj'}\mathcal{E}^{(H)}_{\nu}(\mathbf{k})$, where

$$\mathcal{E}^{(H)}_{\nu}(\mathbf{k}) = \nu\sum_{\mathbf{R}} t^{(H)}_{\mathbf{R}} e^{i(\mathbf{k}-\mathbf{q}_1)\cdot\mathbf{R}}, \tag{69}$$

and the hopping amplitudes also decay rapidly with distance, as displayed in Fig. 5(b).

$t^{(F)}_{\mathbf{R}}/\frac{e^2}{\epsilon L_m}$
$\xi = 5L_m$

-4.405×10^{-5} -1.22×10^{-4} -2.645×10^{-5}
-3.054×10^{-4} -3.076×10^{-4}
-3.052×10^{-4} -2.393×10^{-3} -3.074×10^{-4}
-1.211×10^{-4} -4.797×10^{-3} -4.796×10^{-3} -1.197×10^{-4}
-2.393×10^{-3} -5.302×10^{-2} -2.393×10^{-3}
-2.923×10^{-4} -5.302×10^{-2} -5.302×10^{-2} -2.923×10^{-4}
-6.333×10^{-5} -4.799×10^{-3} 1.714 -4.799×10^{-3} -6.333×10^{-5}
-2.923×10^{-4} -5.302×10^{-2} -5.302×10^{-2} -2.923×10^{-4}
-2.393×10^{-3} -5.302×10^{-2} -2.393×10^{-3}
-1.197×10^{-4} -4.796×10^{-3} -4.797×10^{-3} -1.211×10^{-4}
-3.074×10^{-4} -2.393×10^{-3} -3.052×10^{-4}
-3.076×10^{-4} -3.054×10^{-4}
-2.645×10^{-5} -1.22×10^{-4} -4.405×10^{-5}

(a)

$t^{(H)}_{\mathbf{R}}/\frac{e^2}{\epsilon L_m}$
$\xi = 5L_m$

-2.738×10^{-5} -1.245×10^{-4} -2.738×10^{-5}
-3.176×10^{-4} -3.176×10^{-4}
-3.176×10^{-4} -2.451×10^{-3} -3.176×10^{-4}
-1.245×10^{-4} -4.935×10^{-3} -4.935×10^{-3} -1.245×10^{-4}
-2.451×10^{-3} -5.233×10^{-2} -2.451×10^{-3}
-3.176×10^{-4} -5.233×10^{-2} -5.233×10^{-2} -3.176×10^{-4}
-2.738×10^{-5} -4.935×10^{-3} 3.325×10^{-1} -4.935×10^{-3} -2.738×10^{-5}
-3.176×10^{-4} -5.233×10^{-2} -5.233×10^{-2} -3.176×10^{-4}
-2.451×10^{-3} -5.233×10^{-2} -2.451×10^{-3}
-1.245×10^{-4} -4.935×10^{-3} -4.935×10^{-3} -1.245×10^{-4}
-3.176×10^{-4} -2.451×10^{-3} -3.176×10^{-4}
-3.176×10^{-4} -3.176×10^{-4}
-2.738×10^{-5} -1.245×10^{-4} -2.738×10^{-5}

(b)

FIG. 5. The hopping constants, defined in Eq. (68) for the (a) exchange term, and Eq. (69) for the (b) direct term, on the triangular sublattice of the honeycomb moiré lattice with the screening gate separation $\xi = 5L_m$. In both panels, $t^{(F/H)}_{\mathbf{R}}$'s are shown at the position of $\mathbf{R}$ relative to the center of the cluster. Note that the hopping constants are negligibly small for $|\mathbf{R}| > 2L_m$ and that the values of the (non-negligible) off-site hopping amplitudes are very similar.

Combining the above results, we find that the dispersion from Eq. (39) is

$$\mathcal{E}^h(\mathbf{k}) = \mathcal{E}^{(F)}(\mathbf{k}) - \mathcal{E}^{(H)}_{\nu}(\mathbf{k}), \tag{70}$$

$$\mathcal{E}^p(\mathbf{k}) = \mathcal{E}^{(F)}(\mathbf{k}) + \mathcal{E}^{(H)}_{\nu}(\mathbf{k}). \tag{71}$$

Note that the numerical values of the nearest-neighbor hopping constants from the exchange $t^{(F)}_{\mathbf{L}_1}$ and the direct $t^{(H)}_{\mathbf{L}_1}$ are nearly identical. Therefore, for $\nu = 1$, the hole excitations will have a nearly flat dispersion, while the dispersion for the particle steepens by a factor of $\approx$2. Similarly, at $\nu = -1$, the flattening happens when a particle is added, and the approximate bandwidth doubling happens when a hole is added. We see that the effective mass of the excitations that bring the filling closer to the charge neutrality point (holes for $\nu = 1$ and particles for $\nu = -1$) is much larger than the effective mass for the complementary excitations that move the filling away from the charge neutrality point.

For $\nu = 2$ and $\nu = 3$, the hole bands are completely inverted due to this effect and the electron bands get steeper [31,34]. The effective mass is still very large on the hole side.

VI. DEPENDENCE OF THE DISPERSION ON THE RANGE OF THE COULOMB INTERACTION

In order to gain a better understanding of our results, it is useful to rewrite them in terms of $\tilde{w}$ defined in Eq. (56). This is partly because then we can take advantage of the Wannier product $\tilde{w}^{\dagger}_{\mathbf{R},j}(\mathbf{r})\tilde{w}_{\mathbf{R}',j'}(\mathbf{r})$ being purely real, as shown in Eq. (58), and partly because our Wannier states are 2D exponentially localized.

To this end, we have

$$\mathcal{E}^{(F)}_{jj'}(\mathbf{k}) = \sum_{\mathbf{R}\mathbf{R}'} e^{-i(\mathbf{k}-\mathbf{q}_1)\cdot(\mathbf{R}-\mathbf{R}')} \sum_i \frac{1}{2}\int d^2\mathbf{r}d^2\mathbf{r}' V(\mathbf{r}-\mathbf{r}')\left[e^{-i\frac{3}{2}\mathbf{q}_1\cdot\mathbf{R}}\tilde{w}^{\dagger}_{\mathbf{R},j}(\mathbf{r})\tilde{w}_{\mathbf{0},i}(\mathbf{r})\right]\left[\tilde{w}^{\dagger}_{\mathbf{0},i}(\mathbf{r}')\tilde{w}_{\mathbf{R}',j'}(\mathbf{r}')e^{i\frac{3}{2}\mathbf{q}_1\cdot\mathbf{R}'}\right], \tag{72}$$

$$\mathcal{E}^{(H)}_{\nu,jj'}(\mathbf{k}) = \mp\nu \sum_{\mathbf{R}\mathbf{R}'} e^{-i(\mathbf{k}-\mathbf{q}_1)\cdot(\mathbf{R}-\mathbf{R}')} \sum_i \frac{1}{2}\int d^2\mathbf{r}d^2\mathbf{r}' V(\mathbf{r}-\mathbf{r}')\tilde{w}^{\dagger}_{\mathbf{0},i}(\mathbf{r})\tilde{w}_{\mathbf{0},i}(\mathbf{r})\tilde{w}^{\dagger}_{\mathbf{R},j}(\mathbf{r}')\tilde{w}_{\mathbf{R}',j'}(\mathbf{r}')e^{-i\frac{3}{2}\mathbf{q}_1\cdot(\mathbf{R}-\mathbf{R}')}, \tag{73}$$

where $\tilde{w}_{\mathbf{0},i}(\mathbf{r})$ corresponds to the Wannier state centered inside the origin unit cell ($\mathbf{R} = \mathbf{0}$) either at the *AB* or *BA* sites depending on i. Note that at the $\mathbf{\Gamma}$ point, $\mathbf{k} = \mathbf{q}_1$ and the phase factor before the integrals becomes 1. The phase factors $e^{-i\frac{3}{2}\mathbf{q}_1\cdot\mathbf{R}}$, which we intentionally absorbed inside the integrals, are actually purely real and equal to $(-1)^{m_1}$ for $\mathbf{R} = m_1\mathbf{L}_1 + m_2\mathbf{L}_2$, where $m_{1,2}$ are integers. By comparing with Eqs. (68) and (69), we obtain the formula for the hopping constants,

$$t^{(F)}_{\mathbf{R}} = \sum_{\mathbf{R}'} \frac{1}{2}\int d^2\mathbf{r}d^2\mathbf{r}'\, V(\mathbf{r}-\mathbf{r}') \sum_i \left[e^{-i\frac{3}{2}\mathbf{q}_1\cdot\mathbf{R}'}\tilde{w}^{\dagger}_{\mathbf{R}',1}(\mathbf{r})\tilde{w}_{\mathbf{0},i}(\mathbf{r})\right]\left[\tilde{w}^{\dagger}_{\mathbf{0},i}(\mathbf{r}')\tilde{w}_{\mathbf{R}'+\mathbf{R},1}(\mathbf{r}')e^{i\frac{3}{2}\mathbf{q}_1\cdot(\mathbf{R}'+\mathbf{R})}\right], \tag{74}$$

$$t^{(H)}_{\mathbf{R}} = e^{i\frac{3}{2}\mathbf{q}_1\cdot\mathbf{R}} \sum_{\mathbf{R}'} \frac{1}{2}\int d^2\mathbf{r}d^2\mathbf{r}'\, V(\mathbf{r}-\mathbf{r}') \sum_i [\tilde{w}^{\dagger}_{\mathbf{0},i}(\mathbf{r})\tilde{w}_{\mathbf{0},i}(\mathbf{r})][\tilde{w}^{\dagger}_{\mathbf{R}',1}(\mathbf{r}')\tilde{w}_{\mathbf{R}'+\mathbf{R},1}(\mathbf{r}')]. \tag{75}$$

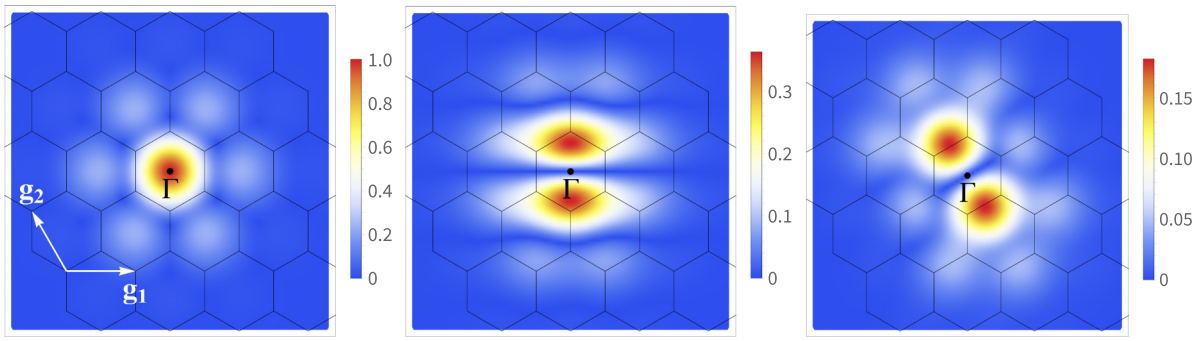

FIG. 6. The plot of $|O_{\mathbf{R},j;\mathbf{R}',j'}(\mathbf{q})|$, where $O_{\mathbf{R},j;\mathbf{R}',j'}(\mathbf{q}) = \int d^2\mathbf{r}\ \tilde{w}^{\dagger}_{\mathbf{R},j}(\mathbf{r})\tilde{w}_{\mathbf{R}',j'}(\mathbf{r})e^{-i\mathbf{q}\cdot\mathbf{r}}$ is the Fourier transform of the product of two Wannier orbitals centered at $\mathbf{R}$, j and $\mathbf{R}'$, j'. The relation between $\tilde{w}_{\mathbf{R},j}(\mathbf{r})$ and $w_{\mathbf{R},j}(\mathbf{r})$ is given in Eq. (56). (a) The Fourier transform of a "monopole"($\mathbf{R} = \mathbf{R}' = \mathbf{0}$ and $j = j' = 1$) is peaked around $\mathbf{\Gamma}$. When centered on different sites, the orthogonality of the Wannier states guarantees that $O_{\mathbf{R},j;\mathbf{R}',j'}(\mathbf{q})$ vanishes as $\mathbf{q} \to 0$. "Dipoles" (b) ($\mathbf{R} = \mathbf{R}' = \mathbf{0}$, $j = 1$ and $j' = 2$) and (c) ($\mathbf{R} = -\mathbf{L}_1$, $\mathbf{R}' = \mathbf{0}$ and $j = j' = 1$) contain two main peaks separated by approximately the primitive reciprocal lattice vector with length $\sim|\mathbf{g}_{1,2}|$; note that the dipoles vanish at $\mathbf{\Gamma}$.

The key insight is to think about each term contributing to the hopping amplitude on a particular bond separately as an electrostatics problem with different charge density distributions. In this way, let us first consider the contribution to $\mathcal{E}^{(F)}_{jj'}(\mathbf{k})$ from $\mathbf{R} = \mathbf{R}'$ (we already established that $j = j'$ is the only nonzero contribution, so we will assume this implicitly). This is the exchange contribution to the on-site term in our effective tight-binding description of the strong coupling single particle dispersion. Thus, within the sum over all terms for which $\mathbf{R} = \mathbf{R}'$, we have one term when $\mathbf{R} = \mathbf{R}' = 0$ and $j = i$ which is equivalent to the electrostatic energy of two coinciding, and 2D localized, "fidget spinners" [see Fig. 4(a)]. The multipole expansion of the (purely real) charge distribution $\tilde{w}^{\dagger}_{0,i}(\mathbf{r})\tilde{w}_{0,i}(\mathbf{r})$ therefore contains a monopole term. In momentum space, this contribution then has the form $\int d^2\mathbf{q}V_{\mathbf{q}}\rho_m(\mathbf{q})\rho_m(-\mathbf{q})$. Because $\rho_m(\mathbf{q})$ is peaked at small $\mathbf{q}$ [see Fig. 6(a)], this integral will be sensitive to the small $\mathbf{q}$ behavior of $V_{\mathbf{q}}$. This is indeed what we see in Fig. 7(a), where we show the dependence of this contribution on the distance to the screening gates ξ, symmetrically positioned above and below the twisted bilayer graphene in which case $V_{\mathbf{q}} = \frac{2\pi e^2}{\epsilon q}\tanh\frac{q\xi}{2}$ for $\mathbf{q} \neq 0$, otherwise at $\mathbf{q} = 0$ it vanishes. Note that even when the gates are $\sim 5L_m$ away from the twisted bilayer, the on-site term is still visibly ξ dependent. The remaining contribution to the on-site $\mathbf{R} = \mathbf{R}'$ term comes from either $\mathbf{R} = \mathbf{R}' \neq 0$ or $i \neq j$. Our electrostatics problem now deals with charge distributions for which the two Wannier states are not centered on the same site, which means they are orthogonal when $\tilde{w}^{\dagger}_{\mathbf{R},j}(\mathbf{r})\tilde{w}_{0,i}(\mathbf{r})$ is integrated over all $\mathbf{r}$; note that $e^{-i\frac{3}{2}\mathbf{q}_1\cdot\mathbf{R}}\tilde{w}^{\dagger}_{\mathbf{R},j}(\mathbf{r})\tilde{w}_{0,i}(\mathbf{r})$ is also purely real for any $\mathbf{r}$. This means that the monopole contribution must be absent.

As shown in Fig. 4, the distributions $e^{-i\frac{3}{2}\mathbf{q}_1\cdot\mathbf{R}}\tilde{w}^{\dagger}_{\mathbf{R},j}(\mathbf{r})\tilde{w}_{0,i}(\mathbf{r})$ indeed look dipolar. In Fourier space, $\rho_d(\mathbf{q})$ must therefore vanish as $\mathbf{q} \to 0$ linearly in $\mathbf{q}\cdot\mathbf{d}$, where $\mathbf{d}$ is the direction of the dipole moment. As a result, the contribution from $\int d^2\mathbf{q}V_{\mathbf{q}}\rho_d(\mathbf{q})\rho_d(-\mathbf{q})$ is much less sensitive to the small $\mathbf{q}$ behavior of $V_{\mathbf{q}}$. This is indeed seen in Fig. 7, where the dependence on ξ from these contributions saturates at a significantly smaller ξ than for the monopole contributions. Note that because our Wannier states are exponentially localized, the contribution to the on-site term in our tight-binding expansion from Wannier states separated by more than $\sqrt{3}L_m$ is negligibly small, and therefore only bonds in the vicinity of the central site need to be considered.

The contribution to the $\mathbf{R} \neq \mathbf{R}'$ hopping terms in our tight-binding description must therefore contain at least one nonmonopole distribution. All such contributions are significantly less sensitive to the small $\mathbf{q}$ behavior of $V_{\mathbf{q}}$ than the monopole-monopole term. This translates to the quicker saturation of the hopping constants with increasing ξ, as shown in Fig. 7(c). In addition, by visually inspecting the charge distribution contributing to the nearest-neighbor hopping displayed in Fig. 4, we see that the contributions coming from the monopole-dipole terms and the nearest-neighbor bond dipole-dipole terms are clearly negative. Since these contributions dominate, this explains why the minimum of the triangular lattice dispersion is at the $\mathbf{\Gamma}$ point. Further hopping constants are also clearly falling off fast with the range of the hopping.

The contribution of the direct term $\mathcal{E}^{(H)}_{\nu,jj'}(\mathbf{k})$ can also be understood using this electrostatics analogy. The sum over $\mathbf{R}$ and $\mathbf{R}'$, while holding $\mathbf{R} - \mathbf{R}'$ fixed, of $\tilde{w}^{\dagger}_{\mathbf{R},j}(\mathbf{r}')\tilde{w}_{\mathbf{R}',j'}(\mathbf{r}')$ leads to a charge distribution which is periodic in space. Therefore, only reciprocal lattice momenta $\mathbf{g}$ contribute to the electrostatic energy. The $\mathbf{q} = 0$ term vanishes because $V_{\mathbf{q}=0}$ vanishes, and the contributions start from $|\mathbf{q}| = |\mathbf{g}_{1,2}| = \frac{4\pi}{\sqrt{3}L_m}$. This probes length scales which are shorter than L_m, which explains the relative insensitivity of the contribution to the tight-binding amplitudes from the direct term shown in Fig. 2(b).

We therefore reach an interesting conclusion: the strong coupling single particle dispersion in the chiral limit is well approximated by the triangular lattice hopping model, with hopping amplitudes which decay rapidly with distance past $2L_m$. The excitation gap, being sensitive to the on-site monopole-monopole term in the exchange contribution, grows with the range of the Coulomb interactions even when $\xi \gtrsim 5L_m$; this is consistent with the recent experiment in

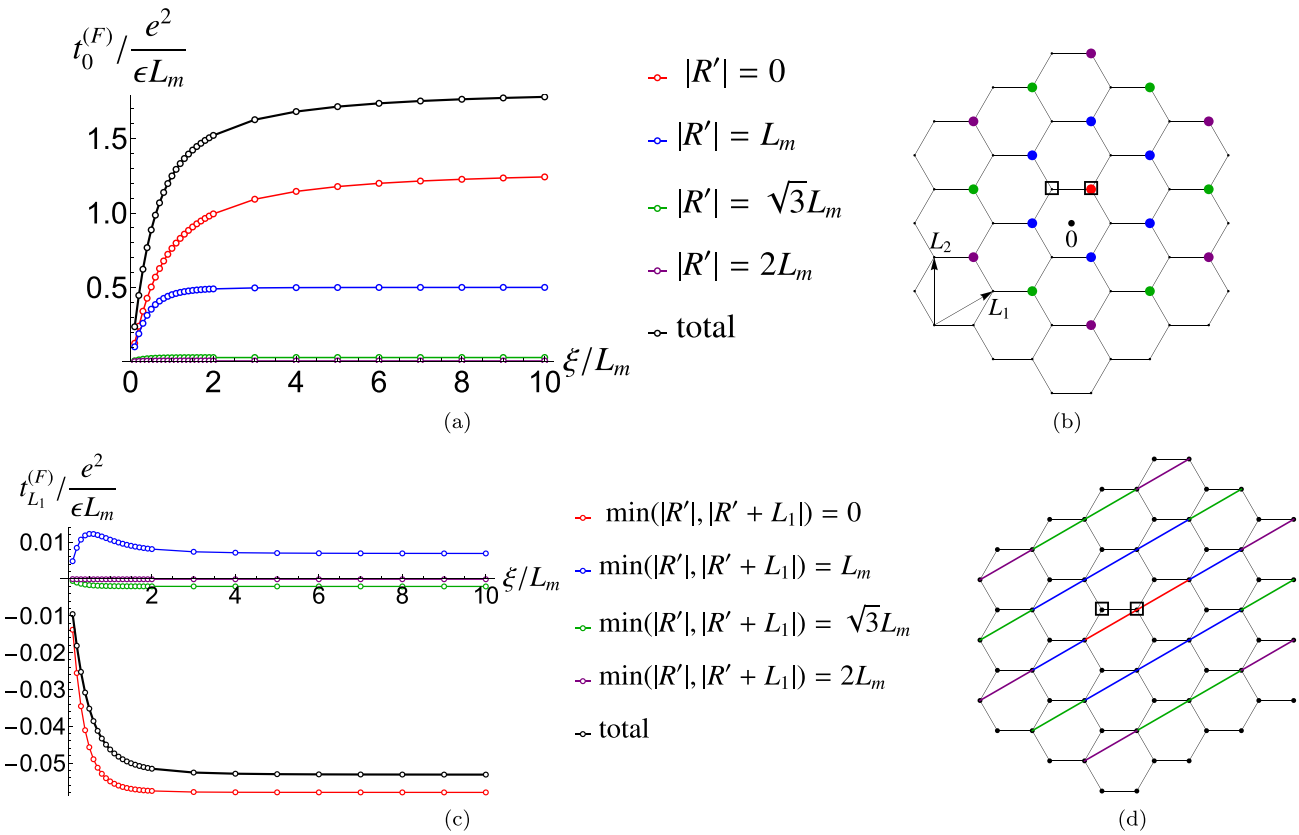

FIG. 7. The exchange contributions to the on-site (above) and the nearest-neighbor hopping (below) terms of the tight-binding model on the triangular lattice. Both the on-site ($\mathbf{R} = \mathbf{0}$) and the nearest-neighbor ($\mathbf{R} = \mathbf{L}_1$) hopping parameters are obtained by summing the contributions from different $\mathbf{R}'$ in Eq. (74). The black curve in (a) shows $t^{(F)}_{\mathbf{R}=\mathbf{0}}$ resulting from the sum over all $\mathbf{R}'$ for different values of ξ. The other colored curves plot the sum over a restricted set of $\mathbf{R}'$s illustrated in (b) using the same color. The two open squares in (b) illustrate the term $\tilde{w}_{\mathbf{0},i}(\mathbf{r})\tilde{w}^{\dagger}_{\mathbf{0},i}(\mathbf{r}')$ appearing in Eq. (74) for $i = 1$ (right open square) and $i = 2$ (left open square). Each term contributing to the sum over $\mathbf{R}'$ and the sum over i for $\mathbf{R} = \mathbf{0}$ is then represented by connecting one of the open squares to one of the colored solid dots in (b), with the corresponding charge distributions illustrated in Fig. 4. Similarly, the colored curves of $t^{(F)}_{\mathbf{R}=\mathbf{L}_1}$ in (c) correspond to those contributions to the sum over $\mathbf{R}'$ and i in Eq. (74) that are obtained by connecting one of the open squares to the two ends of each colored bond $(\mathbf{R}', \mathbf{R}' + \mathbf{L}_1)$ in (d).

which the excitation gap becomes larger as the small momentum part of the interaction $V_{\mathbf{q}}$ increases [41]. On the other hand, the remaining hopping constants are largely insensitive to the range for $\xi \gtrsim L_m$, implying that the effective mass depends on the range of the interaction much more weakly for realistic placement of the screening gates.

VII. SUMMARY

In this paper, we provided a detailed analysis of the strong coupling dispersion in the chiral limit $w_0/w_1 = 0$. We did so first in the Bloch basis and then using 2D exponentially localized Wannier states which transform simply under valley U(1) symmetry, time reversal symmetry, the unitary particle-hole symmetry P, the combination of the chiral particle-hole symmetry, twofold rotation about the axis perpendicular to the plane of the twisted bilayer, and time reversal $\mathcal{C}C_2\mathcal{T}$, as well as $C_2'\mathcal{T}$ [in-plane twofold axis shown in Fig. 1(a) followed by the time reversal] and threefold rotation about the perpendicular C_3 symmetries. The $C_2\mathcal{T}$ symmetry remains obstructed; this should not be taken to mean that it is absent, given that the transformation from Bloch to 2D exponentially localized Wannier states is perfectly unitary. Rather, the $C_2\mathcal{T}$ symmetry is not explicit. It can, in principle, be recovered exponentially fast along the lines outlined in Ref. [9].

The 2D exponentially localized Wannier description allows us to understand why the strong coupling single particle dispersion in the chiral limit is well described by the nearest-neighbor hopping problem on the *triangular* lattice, with a gate distance sensitive on-site term. The negative nearest-neighbor hopping term, which is expected from the real space shape of the overlaps shown in Fig. 4, explains why the minimum of this spectrum is at the $\mathbf{\Gamma}$ point. These features are not easy to understand directly in the Bloch basis.

This work, therefore, highlights not only the ability to, in principle, construct the 2D localized Wannier basis for the chiral limit of the magic-angle twisted bilayer graphene narrow bands, but also their practical utility in understanding nontrivial features of the strong coupling excitation spectra. Thus, complementing the Bloch basis calculations with the Wannier basis analysis provides a more powerful way to understand the complexity of the correlated electrons in topologically nontrivial narrow bands.

ACKNOWLEDGMENTS

We would like to thank Professor B. Andrei Bernevig for valuable discussions. O.V. is supported by NSF Grant No. DMR-1916958 and partially by the National High Magnetic Field Laboratory through NSF Grant No. DMR-1157490 and the State of Florida. J.K. is supported by NSFC Grant No. 12074276 and the Priority Academic Program Development (PAPD) of Jiangsu Higher Education Institutions.

APPENDIX A: DETAILED DERIVATION OF THE SYMMETRIES OF THE WANNIER STATES

The exponentially localized Wannier states are

$$w_{\mathbf{R},j}(\mathbf{r}) = \frac{1}{\sqrt{N_{uc}}}\sum_{m,\mathbf{k}} e^{-i\mathbf{k}\cdot\mathbf{R}}\Phi_{m,\mathbf{k}}(\mathbf{r})\mathrm{UP}\left[\int d^2\mathbf{r}'\Phi^\dagger_{m,\mathbf{k}}(\mathbf{r}')h_j(\mathbf{r}')\right], \tag{A1}$$

where the triangular moiré lattice is spanned by $\mathbf{R} = m_1\mathbf{L}_1 + m_2\mathbf{L}_2$, with integer $m_{1,2}$, and UP stands for the "unitary part" of the 2×2 matrix $A_{mj}(\mathbf{k})$ [Eq. (44)]. As defined in the main text,

$$h_1(\mathbf{r}) = \begin{pmatrix} i\\ 0\\ 0\\ -\varepsilon^* \end{pmatrix}\delta(\mathbf{r}-\mathbf{r}_{AB}), \quad h_2(\mathbf{r}) = \varepsilon^* C_2' T h_1(\mathbf{r}) = \begin{pmatrix} 0\\ -1\\ -i\varepsilon^*\\ 0 \end{pmatrix}\delta(\mathbf{r}-\mathbf{r}_{BA}), \tag{A2}$$

where $\mathbf{r}_{AB} = \frac{1}{3}(\mathbf{L}_1+\mathbf{L}_2)$, $\mathbf{r}_{BA} = \frac{1}{3}(2\mathbf{L}_2-\mathbf{L}_1)$, $\varepsilon = e^{2\pi i/3} = e^{-i\mathbf{q}_1\cdot\mathbf{r}_{AB}} = e^{-i\mathbf{q}_1\cdot\mathbf{r}_{BA}}$, and $\delta(\mathbf{r})$ is the 2D Dirac δ function.

1. Action of the symmetry operation *P*

This symmetry operation was discussed in detail in Sec. II. Its action on the Wannier state is

$$-i\mu_y w_{\mathbf{R},j}(-\mathbf{r}) = \frac{1}{\sqrt{N_{uc}}}\sum_{m,\mathbf{k}} e^{-i\mathbf{k}\cdot\mathbf{R}}(-i\mu_y)\Phi_{m,\mathbf{k}}(-\mathbf{r})\mathrm{UP}\left[\int d^2\mathbf{r}'\Phi^\dagger_{m,\mathbf{k}}(\mathbf{r}')h_j(\mathbf{r}')\right] \tag{A3}$$

$$= \frac{1}{\sqrt{N_{uc}}}\sum_{m,\mathbf{k}} e^{-i\mathbf{k}\cdot\mathbf{R}}(-i\mu_y)\Phi_{m,\mathbf{k}}(-\mathbf{r})\mathrm{UP}\left[\int d^2\mathbf{r}'\Phi^\dagger_{m,\mathbf{k}}(-\mathbf{r}')i\mu_y(-i\mu_y)h_j(-\mathbf{r}')\right] \tag{A4}$$

$$= \frac{1}{\sqrt{N_{uc}}}\sum_{m,\mathbf{k}} e^{-i\mathbf{k}\cdot\mathbf{R}}\Phi_{m,-\mathbf{k}-\mathbf{q}_1}(\mathbf{r})\mathrm{UP}\left[\int d^2\mathbf{r}'\Phi^\dagger_{m,-\mathbf{k}-\mathbf{q}_1}(\mathbf{r}')(-i\mu_y)h_j(-\mathbf{r}')\right] \tag{A5}$$

$$= \frac{1}{\sqrt{N_{uc}}}\sum_{m,\mathbf{k}} e^{i(\mathbf{k}+\mathbf{q}_1)\cdot\mathbf{R}}\Phi_{m,\mathbf{k}}(\mathbf{r})\mathrm{UP}\left[\int d^2\mathbf{r}'\Phi^\dagger_{m,\mathbf{k}}(\mathbf{r}')(-i\mu_y)h_j(-\mathbf{r}')\right]. \tag{A6}$$

Going from (A4) to (A5), we used Eq. (19) and the fact that any $\mathbf{k}$-dependent phase factors acquired by Φ are canceled by those coming from $\Phi^\dagger$ because they can be taken outside the UP (as is readily seen when considering SVD). Substituting our trial function (45) and (46), we have

$$(-i\mu_y)h_1(-\mathbf{r}') = \begin{pmatrix} 0\\ \varepsilon^*\\ i\\ 0 \end{pmatrix}\delta(\mathbf{r}+\mathbf{r}_{AB}) = \begin{pmatrix} -\varepsilon^* & 0 & 0 & 0\\ 0 & -\varepsilon^* & 0 & 0\\ 0 & 0 & -\varepsilon & 0\\ 0 & 0 & 0 & -\varepsilon \end{pmatrix} h_2(\mathbf{r}+\mathbf{L}_2), \tag{A7}$$

$$(-i\mu_y)h_2(-\mathbf{r}') = \begin{pmatrix} i\varepsilon^*\\ 0\\ 0\\ -1 \end{pmatrix}\delta(\mathbf{r}+\mathbf{r}_{BA}) = \begin{pmatrix} \varepsilon^* & 0 & 0 & 0\\ 0 & \varepsilon^* & 0 & 0\\ 0 & 0 & \varepsilon & 0\\ 0 & 0 & 0 & \varepsilon \end{pmatrix} h_1(\mathbf{r}+\mathbf{L}_2). \tag{A8}$$

So,

$$-i\mu_y w_{\mathbf{R},1}(-\mathbf{r}) = -\frac{1}{\sqrt{N_{uc}}}\sum_{m,\mathbf{k}} e^{i(\mathbf{k}+\mathbf{q}_1)\cdot\mathbf{R}}\Phi_{m,\mathbf{k}}(\mathbf{r})\mathrm{UP}\left[\int d^2\mathbf{r}'\Phi^\dagger_{m,\mathbf{k}}(\mathbf{r}')\begin{pmatrix} \varepsilon^* & 0 & 0 & 0\\ 0 & \varepsilon^* & 0 & 0\\ 0 & 0 & \varepsilon & 0\\ 0 & 0 & 0 & \varepsilon \end{pmatrix} h_2(\mathbf{r}'+\mathbf{L}_2)\right], \tag{A9}$$

$$-i\mu_y w_{\mathbf{R},2}(-\mathbf{r}) = \frac{1}{\sqrt{N_{uc}}}\sum_{m,\mathbf{k}} e^{i(\mathbf{k}+\mathbf{q}_1)\cdot\mathbf{R}}\Phi_{m,\mathbf{k}}(\mathbf{r})\mathrm{UP}\left[\int d^2\mathbf{r}'\Phi^\dagger_{m,\mathbf{k}}(\mathbf{r}')\begin{pmatrix} \varepsilon^* & 0 & 0 & 0\\ 0 & \varepsilon^* & 0 & 0\\ 0 & 0 & \varepsilon & 0\\ 0 & 0 & 0 & \varepsilon \end{pmatrix} h_1(\mathbf{r}'+\mathbf{L}_2)\right]. \tag{A10}$$

Shifting the overlap integral and using the definition (4), we have

$$\int d^2\mathbf{r}'\Phi^\dagger_{m,\mathbf{k}}(\mathbf{r}')\begin{pmatrix}\varepsilon^* & 0 & 0 & 0\\ 0 & \varepsilon^* & 0 & 0\\ 0 & 0 & \varepsilon & 0\\ 0 & 0 & 0 & \varepsilon\end{pmatrix}h_j(\mathbf{r}'+\mathbf{L}_2) = \int d^2\mathbf{r}'\Phi^\dagger_{m,\mathbf{k}}(\mathbf{r}'-\mathbf{L}_2)\begin{pmatrix}\varepsilon^* & 0 & 0 & 0\\ 0 & \varepsilon^* & 0 & 0\\ 0 & 0 & \varepsilon & 0\\ 0 & 0 & 0 & \varepsilon\end{pmatrix}h_j(\mathbf{r}') \tag{A11}$$

$$= e^{i\mathbf{k}\cdot\mathbf{L}_2}\int d^2\mathbf{r}'\Phi^\dagger_{m,\mathbf{k}}(\mathbf{r}')\begin{pmatrix}1 & 0 & 0 & 0\\ 0 & 1 & 0 & 0\\ 0 & 0 & e^{i\mathbf{q}_1\mathbf{L}_2} & 0\\ 0 & 0 & 0 & e^{i\mathbf{q}_1\mathbf{L}_2}\end{pmatrix}\begin{pmatrix}\varepsilon^* & 0 & 0 & 0\\ 0 & \varepsilon^* & 0 & 0\\ 0 & 0 & \varepsilon & 0\\ 0 & 0 & 0 & \varepsilon\end{pmatrix}h_j(\mathbf{r}') = \varepsilon^* e^{i\mathbf{k}\cdot\mathbf{L}_2}\int d^2\mathbf{r}'\Phi^\dagger_{m,\mathbf{k}}(\mathbf{r}')h_j(\mathbf{r}'). \tag{A12}$$

Substituting into (A9) and (A10), we finally have

$$-i\mu_y w_{\mathbf{R},1}(-\mathbf{r}) = -\varepsilon^* e^{i\mathbf{q}_1\cdot\mathbf{R}} w_{-\mathbf{R}-\mathbf{L}_2,2}(\mathbf{r}), \tag{A13}$$

$$-i\mu_y w_{\mathbf{R},2}(-\mathbf{r}) = \varepsilon^* e^{i\mathbf{q}_1\cdot\mathbf{R}} w_{-\mathbf{R}-\mathbf{L}_2,1}(\mathbf{r}), \tag{A14}$$

which match the result stated in the main text: Eqs. (47) and (48).

2. Action of the symmetry operation $\mathcal{C}C_2T$

$$\sigma_z\sigma_x w^*_{\mathbf{R},j}(-\mathbf{r}) = \frac{1}{\sqrt{N_{uc}}}\sum_{m,\mathbf{k}} e^{i\mathbf{k}\cdot\mathbf{R}}\sigma_z\sigma_x\Phi^*_{m,\mathbf{k}}(-\mathbf{r})\mathrm{UP}\left[\int d^2\mathbf{r}'\Phi^\dagger_{m,\mathbf{k}}(\mathbf{r}')h_j(\mathbf{r}')\right]^* \tag{A15}$$

$$= \frac{1}{\sqrt{N_{uc}}}\sum_{m,\mathbf{k}} e^{i\mathbf{k}\cdot\mathbf{R}}i\sigma_y\Phi^*_{m,\mathbf{k}}(-\mathbf{r})\mathrm{UP}\left[\int d^2\mathbf{r}'\Phi^T_{m,\mathbf{k}}(-\mathbf{r}')(-i\sigma_y)i\sigma_y h^*_j(-\mathbf{r}')\right] \tag{A16}$$

$$= \frac{1}{\sqrt{N_{uc}}}\sum_{m,\mathbf{k}} e^{i\mathbf{k}\cdot\mathbf{R}}\Phi_{m,\mathbf{k}}(\mathbf{r})\mathrm{UP}\left[\int d^2\mathbf{r}'\Phi^\dagger_{m,\mathbf{k}}(\mathbf{r}')i\sigma_y h^*_j(-\mathbf{r}')\right], \tag{A17}$$

$$i\sigma_y h^*_1(-\mathbf{r}) = \begin{pmatrix}0\\ i\\ \varepsilon\\ 0\end{pmatrix}\delta(\mathbf{r}+\mathbf{r}_{AB}) = \begin{pmatrix}-i & 0 & 0 & 0\\ 0 & -i & 0 & 0\\ 0 & 0 & -i\varepsilon^* & 0\\ 0 & 0 & 0 & -i\varepsilon^*\end{pmatrix}h_2(\mathbf{r}+\mathbf{L}_2), \tag{A18}$$

$$i\sigma_y h^*_2(-\mathbf{r}) = \begin{pmatrix}-1\\ 0\\ 0\\ -i\varepsilon\end{pmatrix}\delta(\mathbf{r}+\mathbf{r}_{BA}) = \begin{pmatrix}i & 0 & 0 & 0\\ 0 & i & 0 & 0\\ 0 & 0 & i\varepsilon^* & 0\\ 0 & 0 & 0 & i\varepsilon^*\end{pmatrix}h_1(\mathbf{r}+\mathbf{L}_2), \tag{A19}$$

$$\sigma_z\sigma_x w^*_{\mathbf{R},1(2)}(-\mathbf{r}) = \frac{\mp i}{\sqrt{N_{uc}}}\sum_{m,\mathbf{k}} e^{i\mathbf{k}\cdot\mathbf{R}}\Phi_{m,\mathbf{k}}(\mathbf{r})\mathrm{UP}\left[\int d^2\mathbf{r}'\Phi^\dagger_{m,\mathbf{k}}(\mathbf{r}')\begin{pmatrix}1 & 0 & 0 & 0\\ 0 & 1 & 0 & 0\\ 0 & 0 & \varepsilon^* & 0\\ 0 & 0 & 0 & \varepsilon^*\end{pmatrix}h^*_{2(1)}(\mathbf{r}'+\mathbf{L}_2)\right] \tag{A20}$$

$$= \frac{\mp i}{\sqrt{N_{uc}}}\sum_{m,\mathbf{k}} e^{i\mathbf{k}\cdot(\mathbf{R}+\mathbf{L}_2)}\Phi_{m,\mathbf{k}}(\mathbf{r})\mathrm{UP}\left[\int d^2\mathbf{r}'\Phi^\dagger_{m,\mathbf{k}}(\mathbf{r}')\begin{pmatrix}1 & 0 & 0 & 0\\ 0 & 1 & 0 & 0\\ 0 & 0 & e^{i\mathbf{q}_1\cdot\mathbf{L}_2} & 0\\ 0 & 0 & 0 & e^{i\mathbf{q}\cdot\mathbf{L}_2}\end{pmatrix}\begin{pmatrix}1 & 0 & 0 & 0\\ 0 & 1 & 0 & 0\\ 0 & 0 & \varepsilon^* & 0\\ 0 & 0 & 0 & \varepsilon^*\end{pmatrix}h^*_{2(1)}(\mathbf{r}')\right] \tag{A21}$$

$$= \mp i w_{-\mathbf{R}-\mathbf{L}_2,2(1)}(\mathbf{r}). \tag{A22}$$

This matches the result in Eqs. (49) and (50).

APPENDIX B: RELATION BETWEEN DIFFERENT U(4) ROTATIONS

In order to make explicit the relation between different U(4) symmetries mentioned in the main text, we start by recalling the definition of the fermion operators in different bases,

$$\chi_\sigma(\mathbf{r}) = \begin{pmatrix}\psi_\sigma(\mathbf{r})\\ \phi_\sigma(\mathbf{r})\end{pmatrix} = \sum_{\mathbf{k}}\sum_{n=n\pm}\begin{pmatrix}\Psi_{n,\mathbf{k}}(\mathbf{r})d_{\sigma,\mathbf{K},n,\mathbf{k}}\\ \Psi^*_{n,\mathbf{k}}(\mathbf{r})d_{\sigma,\mathbf{K}',n,-\mathbf{k}-\mathbf{q}_1}\end{pmatrix} = \sum_{\mathbf{k}}\sum_{\lambda=\pm}\begin{pmatrix}\Phi_{\lambda,\mathbf{k}}(\mathbf{r})e_{\sigma,\mathbf{K},\lambda,\mathbf{k}}\\ e^{i\alpha^C_{\mathbf{k}}}\Phi^*_{\lambda,\mathbf{k}}(\mathbf{r})e_{\sigma,\mathbf{K}',-\lambda,-\mathbf{k}-\mathbf{q}_1}\end{pmatrix}$$

$$= \sum_{\mathbf{R}}\sum_{j=1,2}\begin{pmatrix}\tilde{w}_{\mathbf{R},j}(\mathbf{r})f_{\sigma,\mathbf{K},j,\mathbf{R}}\\ \tilde{w}^*_{\mathbf{R},j}(\mathbf{r})f_{\sigma,\mathbf{K}',j,\mathbf{R}}\end{pmatrix}. \tag{B1}$$

The relation between the basis functions is

$$\Phi_{\pm,\mathbf{k}}(\mathbf{r}) = \frac{1}{\sqrt{2}}(1_2\sigma_z \pm 1_4)\Psi_{n+,\mathbf{k}}(\mathbf{r}) = \frac{1}{\sqrt{2}}\left[e^{i\alpha^{\mathcal{C}}_{\mathbf{k}}}\Psi_{n-,\mathbf{k}}(\mathbf{r}) \pm \Psi_{n+,\mathbf{k}}(\mathbf{r})\right], \tag{B2}$$

$$\tilde{w}_{\mathbf{R},j}(\mathbf{r}) = e^{i\frac{\pi}{12}}e^{-\frac{i}{2}\mathbf{q}_1\cdot\mathbf{R}}w_{\mathbf{R},j}(\mathbf{r}) = \frac{1}{\sqrt{N_{uc}}}e^{i\frac{\pi}{12}}\sum_{\mathbf{k}}\sum_{m=\pm}e^{-i(\mathbf{k}+\frac{\mathbf{q}_1}{2})\cdot\mathbf{R}}\Phi_{m,\mathbf{k}}(\mathbf{r})\mathcal{U}_{mj}(\mathbf{k}). \tag{B3}$$

Let us start with the first equality and read off the coefficients using the orthogonality of $\Psi's$,

$$d_{\sigma,\mathbf{K},n+,\mathbf{k}} = \frac{1}{\sqrt{2}}(e_{\sigma,\mathbf{K},+,\mathbf{k}} - e_{\sigma,\mathbf{K},-,\mathbf{k}}), \tag{B4}$$

$$d_{\sigma,\mathbf{K},n-,\mathbf{k}} = \frac{e^{i\alpha^{\mathcal{C}}_{\mathbf{k}}}}{\sqrt{2}}(e_{\sigma,\mathbf{K},+,\mathbf{k}} + e_{\sigma,\mathbf{K},-,\mathbf{k}}), \tag{B5}$$

$$d_{\sigma,\mathbf{K}',n+,-\mathbf{k}-\mathbf{q}_1} = \frac{e^{i\alpha^{\mathcal{C}}_{\mathbf{k}}}}{\sqrt{2}}(e_{\sigma,\mathbf{K}',-,-\mathbf{k}-\mathbf{q}_1} - e_{\sigma,\mathbf{K}',+,-\mathbf{k}-\mathbf{q}_1}), \tag{B6}$$

$$d_{\sigma,\mathbf{K}',n-,-\mathbf{k}-\mathbf{q}_1} = \frac{1}{\sqrt{2}}(e_{\sigma,\mathbf{K}',-,-\mathbf{k}-\mathbf{q}_1} + e_{\sigma,\mathbf{K}',+,-\mathbf{k}-\mathbf{q}_1}), \tag{B7}$$

where we used

$$\Psi^*_{n+,\mathbf{k}}(\mathbf{r})d_{\sigma,\mathbf{K}',n+,-\mathbf{k}-\mathbf{q}_1} + \Psi^*_{n-,\mathbf{k}}(\mathbf{r})d_{\sigma,\mathbf{K}',n-,-\mathbf{k}-\mathbf{q}_1} = e^{i\alpha^{\mathcal{C}}_{\mathbf{k}}}\Phi^*_{+,\mathbf{k}}(\mathbf{r})e_{\sigma,\mathbf{K}',-,-\mathbf{k}-\mathbf{q}_1} + e^{i\alpha^{\mathcal{C}}_{\mathbf{k}}}\Phi^*_{-,\mathbf{k}}(\mathbf{r})e_{\sigma,\mathbf{K}',+,-\mathbf{k}-\mathbf{q}_1}, \tag{B8}$$

$$\begin{pmatrix} d_{\sigma,\mathbf{K},n+,\mathbf{k}} \\ d_{\sigma,\mathbf{K},n-,\mathbf{k}} \\ d_{\sigma,\mathbf{K}',n+,\mathbf{k}} \\ d_{\sigma,\mathbf{K}',n-,\mathbf{k}} \end{pmatrix} = \frac{1}{\sqrt{2}}\begin{pmatrix} 1 & -1 & 0 & 0 \\ e^{i\alpha^{\mathcal{C}}_{\mathbf{k}}} & e^{i\alpha^{\mathcal{C}}_{\mathbf{k}}} & 0 & 0 \\ 0 & 0 & e^{i\alpha^{\mathcal{C}}_{-\mathbf{k}-\mathbf{q}_1}} & -e^{i\alpha^{\mathcal{C}}_{-\mathbf{k}-\mathbf{q}_1}} \\ 0 & 0 & 1 & 1 \end{pmatrix}\begin{pmatrix} e_{\sigma,\mathbf{K},+,\mathbf{k}} \\ e_{\sigma,\mathbf{K},-,\mathbf{k}} \\ e_{\sigma,\mathbf{K}',-,\mathbf{k}} \\ e_{\sigma,\mathbf{K}',+,\mathbf{k}} \end{pmatrix}. \tag{B9}$$

Now, if $\mathbf{k} = \mathbf{\Gamma}$, then $e^{i\alpha^{\mathcal{C}}_{\mathbf{k}}} = e^{i\alpha^{\mathcal{C}}_{-\mathbf{k}-\mathbf{q}_1}} = i$. If $\mathbf{k} \neq \mathbf{\Gamma}$, then $e^{i\alpha^{\mathcal{C}}_{\mathbf{k}}} = e^{i\alpha^{\mathcal{C}}_{-\mathbf{k}-\mathbf{q}_1}} = -i$.

By explicit calculation, we find that

$$\left[G^{nc-\text{flat}}_{U(4)}, \frac{1}{\sqrt{2}}\begin{pmatrix} 1 & -1 & 0 & 0 \\ e^{i\alpha^{\mathcal{C}}_{\mathbf{k}}} & e^{i\alpha^{\mathcal{C}}_{\mathbf{k}}} & 0 & 0 \\ 0 & 0 & e^{i\alpha^{\mathcal{C}}_{-\mathbf{k}-\mathbf{q}_1}} & -e^{i\alpha^{\mathcal{C}}_{-\mathbf{k}-\mathbf{q}_1}} \\ 0 & 0 & 1 & 1 \end{pmatrix}\right] = 0, \tag{B10}$$

where $G^{nc-flat}_{U(4)}$ is any of the nonchiral flat generators 1_4, $\tau_z 1_2$, $\tau_y\tilde{\sigma}_y$, or $\tau_x\tilde{\sigma}_y$. Writing out these matrices explicitly, we can see that if we rotate the Chern $+1$ basis using $\alpha\cdot(1_2, \tau_z, -\tau_x, \tau_y)$, then we must simultaneously rotate Chern -1 using $\alpha\cdot(1_2, \tau_z, \tau_x, -\tau_y)$. The spin SU(2) follows trivially from the tensor product.

The second equality implies

$$f_{\sigma,\mathbf{K},j,\mathbf{R}} = \sum_{\mathbf{k}}\sum_{\lambda=\pm}\int d^2\mathbf{r}\tilde{w}^{\dagger}_{\mathbf{R},j}(\mathbf{r})\Phi_{\lambda,\mathbf{k}}(\mathbf{r})e_{\sigma,\mathbf{K},\lambda,\mathbf{k}}, \tag{B11}$$

$$f_{\sigma,\mathbf{K}',j,\mathbf{R}} = \sum_{\mathbf{k}}\sum_{\lambda=\pm}e^{i\alpha^{\mathcal{C}}_{\mathbf{k}}}\int d^2\mathbf{r}\tilde{w}^{T}_{\mathbf{R},j}(\mathbf{r})\Phi^*_{\lambda,\mathbf{k}}(\mathbf{r})e_{\sigma,\mathbf{K}',-\lambda,-\mathbf{k}-\mathbf{q}_1}. \tag{B12}$$

Therefore,

$$f_{\sigma,\mathbf{K},j,\mathbf{R}} = \frac{1}{\sqrt{N_{uc}}}\sum_{\mathbf{k}}\sum_{\lambda=\pm}e^{-i\frac{\pi}{12}}e^{i(\mathbf{k}+\frac{\mathbf{q}_1}{2})\cdot\mathbf{R}}\mathcal{U}^*_{\lambda j}(\mathbf{k})e_{\sigma,\mathbf{K},\lambda,\mathbf{k}}, \tag{B13}$$

$$f_{\sigma,\mathbf{K}',j,\mathbf{R}} = \frac{1}{\sqrt{N_{uc}}}\sum_{\mathbf{k}}\sum_{\lambda=\pm}e^{i\alpha^{\mathcal{C}}_{\mathbf{k}}}e^{i\frac{\pi}{12}}e^{-i(\mathbf{k}+\frac{\mathbf{q}_1}{2})\cdot\mathbf{R}}\mathcal{U}_{\lambda j}(\mathbf{k})e_{\sigma,\mathbf{K}',-\lambda,-\mathbf{k}-\mathbf{q}_1} \tag{B14}$$

$$= \frac{1}{\sqrt{N_{uc}}}\sum_{\mathbf{k}}\sum_{\lambda=\pm}e^{i\alpha^{\mathcal{C}}_{-\mathbf{k}-\mathbf{q}_1}}e^{i\frac{\pi}{12}}e^{i(\mathbf{k}+\frac{\mathbf{q}_1}{2})\cdot\mathbf{R}}\mathcal{U}_{-\lambda,j}(-\mathbf{k}-\mathbf{q}_1)e_{\sigma,\mathbf{K}',\lambda,\mathbf{k}}. \tag{B15}$$

Now,

$$e^{i\alpha^{\mathcal{C}}_{-\mathbf{k}-\mathbf{q}_1}}\mathcal{U}_{-\lambda,j}(-\mathbf{k}-\mathbf{q}_1) = e^{i\alpha^{\mathcal{C}}_{-\mathbf{k}-\mathbf{q}_1}}\text{UP}\left[\int d^2\mathbf{r}\Phi^{\dagger}_{-\lambda,-\mathbf{k}-\mathbf{q}_1}(\mathbf{r})h_j(\mathbf{r})\right]. \tag{B16}$$

But,

$$e^{i\alpha^C_{-\mathbf{k}-\mathbf{q}_1}}\Phi^\dagger_{-\lambda,-\mathbf{k}-\mathbf{q}_1}(\mathbf{r}) = -\Phi^T_{\lambda,\mathbf{k}}(\mathbf{r})\mu_y\sigma_y. \tag{B17}$$

So,

$$e^{i\alpha^C_{-\mathbf{k}-\mathbf{q}_1}}\mathcal{U}_{-\lambda,j}(-\mathbf{k}-\mathbf{q}_1) = -\mathrm{UP}\left[\int d^2\mathbf{r}\Phi^\dagger_{\lambda,\mathbf{k}}(\mathbf{r})\mu_y\sigma_y h^*_j(\mathbf{r})\right]^*, \tag{B18}$$

and, for our choice of the trial states,

$$\mu_y\sigma_y h^*_j(\mathbf{r}) = e^{i\frac{\pi}{6}}h_j(\mathbf{r}). \tag{B19}$$

Therefore,

$$e^{i\alpha^C_{-\mathbf{k}-\mathbf{q}_1}}\mathcal{U}_{-\lambda,j}(-\mathbf{k}-\mathbf{q}_1) = -e^{-i\frac{\pi}{6}}\mathrm{UP}\left[\int d^2\mathbf{r}\Phi^\dagger_{\lambda,\mathbf{k}}(\mathbf{r})h_j(\mathbf{r})\right]^* = -e^{-i\frac{\pi}{6}}\mathcal{U}^*_{\lambda,j}(\mathbf{k}). \tag{B20}$$

Therefore, we get

$$f_{\sigma,\mathbf{K},j,\mathbf{R}} = \frac{1}{\sqrt{N_{uc}}}\sum_{\mathbf{k}}\sum_{\lambda=\pm}e^{-i\frac{\pi}{12}}e^{i(\mathbf{k}+\frac{\mathbf{q}_1}{2})\cdot\mathbf{R}}\mathcal{U}^*_{\lambda j}(\mathbf{k})e_{\sigma,\mathbf{K},\lambda,\mathbf{k}}, \tag{B21}$$

$$f_{\sigma,\mathbf{K}',j,\mathbf{R}} = -\frac{1}{\sqrt{N_{uc}}}\sum_{\mathbf{k}}\sum_{\lambda=\pm}e^{i\frac{\pi}{12}}e^{i(\mathbf{k}+\frac{\mathbf{q}_1}{2})\cdot\mathbf{R}}e^{-i\frac{\pi}{6}}\mathcal{U}^*_{\lambda,j}(\mathbf{k})e_{\sigma,\mathbf{K}',\lambda,\mathbf{k}}. \tag{B22}$$

Or, expressed in a matrix form,

$$\begin{pmatrix} f_{\sigma,\mathbf{K},j,\mathbf{R}} \\ f_{\sigma,\mathbf{K}',j,\mathbf{R}}\end{pmatrix} = \frac{1}{\sqrt{N_{uc}}}\sum_{\mathbf{k}}\sum_{\lambda=\pm}e^{-i\frac{\pi}{12}}e^{i(\mathbf{k}+\frac{\mathbf{q}_1}{2})\cdot\mathbf{R}}\mathcal{U}^*_{\lambda j}(\mathbf{k})\begin{pmatrix}1 & 0\\ 0 & -1\end{pmatrix}\begin{pmatrix} e_{\sigma,\mathbf{K},\lambda,\mathbf{k}} \\ e_{\sigma,\mathbf{K}',\lambda,\mathbf{k}}\end{pmatrix}. \tag{B23}$$

So, if we perform a valley U(2) rotation $e^{i\alpha\cdot(1,\tau_z,\tau_x,\tau_y)}$ on f's, then we are performing $e^{i\alpha\cdot(1,\tau_z,-\tau_x,-\tau_y)}$ rotation on e's *independent* of λ. Clearly, the two Chern numbers are rotated by the same angle. This is unlike in the previous example of the nonchiral flat limit where the Chern $+1$ and Chern -1 were rotated by angle vectors which are related by mirror reflection about the z axis.

[1] R. Bistritzer and A. H. MacDonald, Moire bands in twisted double-layer graphene, Proc. Natl. Acad. Sci. USA **108**, 12233 (2011).

[2] Y. Cao, V. Fatemi, A. Demir, S. Fang, S. L. Tomarken, J. Y. Luo, J. D. Sanchez-Yamagishi, K. Watanabe, T. Taniguchi, E. Kaxiras, R. C. Ashoori, and P. Jarillo-Herrero, Correlated insulator behaviour at half-filling in magic-angle graphene superlattices, Nature (London) **556**, 43 (2018).

[3] Y. Cao, V. Fatemi, S. Fang, K. Watanabe, T. Taniguchi, E. Kaxiras, and P. Jarillo-Herrero, Unconventional superconductivity in magic-angle graphene superlattices, Nature (London) **556**, 80 (2018).

[4] M. Yankowitz, S. Chen, H. Polshyn, Y. Zhang, K. Watanabe, T. Taniguchi, D. Graf, A. F. Young, and C. R. Dean, Tuning superconductivity in twisted bilayer graphene, Science **363**, 1059 (2019).

[5] A. L. Sharpe, E. J. Fox, A. W. Barnard, J. Finney, K. Watanabe, T. Taniguchi, M. A. Kastner, and D. Goldhaber-Gordon, Emergent ferromagnetism near three-quarters filling in twisted bilayer graphene, Science **365**, 605 (2019).

[6] M. Serlin, C. L. Tschirhart, H. Polshyn, Y. Zhang, J. Zhu, K. Watanabe, T. Taniguchi, L. Balents, and A. F. Young, Intrinsic quantized anomalous Hall effect in a moire heterostructure, Science **367**, 900 (2019).

[7] C. Brouder, G. Panati, M. Calandra, C. Mourougane, and N. Marzari, Exponential Localization of Wannier Functions in Insulators, Phys. Rev. Lett. **98**, 046402 (2007).

[8] A. A. Soluyanov and D. Vanderbilt, Wannier representation of $\mathbb{Z}_2$ topological insulators, Phys. Rev. B **83**, 035108 (2011).

[9] X. Wang and O. Vafek, Diagnosis of explicit symmetry breaking in the tight-binding constructions for symmetry-protected topological systems, Phys. Rev. B **102**, 075142 (2020).

[10] H. C. Po, L. Zou, A. Vishwanath, and T. Senthil, Origin of Mott Insulating Behavior and Superconductivity in Twisted Bilayer Graphene, Phys. Rev. X **8**, 031089 (2018).

[11] Z. Song, Z. Wang, W. Shi, G. Li, C. Fang, and B. A. Bernevig, All Magic Angles in Twisted Bilayer Graphene are Topological, Phys. Rev. Lett. **123**, 036401 (2019).

[12] B. A. Bernevig, Z. D. Song, N. Regnault, and B. Lian, Twisted bilayer graphene. I. Matrix elements, approximations, perturbation theory, and a $\mathbf{k}\cdot\mathbf{p}$ two-band model, Phys. Rev. B **103**, 205411 (2021).

[13] J. Kang and O. Vafek, Symmetry, Maximally Localized Wannier States, and a Low-Energy Model for Twisted Bilayer Graphene Narrow Bands, Phys. Rev. X **8**, 031088 (2018).

[14] M. Koshino, N. F. Q. Yuan, T. Koretsune, M. Ochi, K. Kuroki, and L. Fu, Maximally Localized Wannier Orbitals and the Extended Hubbard Model for Twisted Bilayer Graphene, Phys. Rev. X **8**, 031087 (2018).

[15] H. C. Po, L. Zou, T. Senthil, and A. Vishwanath, Faithful tight-binding models and fragile topology of magic-angle bilayer graphene, Phys. Rev. B **99**, 195455 (2019).

[16] Z. D. Song, B. Lian, N. Regnault, and B. A. Bernevig, Twisted bilayer graphene. II. Stable symmetry anomaly, Phys. Rev. B **103**, 205412 (2021).

[17] G. Tarnopolsky, A. J. Kruchkov, and A. Vishwanath, Origin of Magic Angles in Twisted Bilayer Graphene, Phys. Rev. Lett. **122**, 106405 (2019).

[18] M. Xie and A. H. MacDonald, Nature of the Correlated Insulator States in Twisted Bilayer Graphene, Phys. Rev. Lett. **124**, 097601 (2020).

[19] S. Liu, E. Khalaf, J. Y. Lee, and A. Vishwanath, Nematic topological semimetal and insulator in magic angle bilayer graphene at charge neutrality, Phys. Rev. Res. **3**, 013033 (2021).

[20] F. Guinea and N. R. Walet, Electrostatic effects, band distortions, and superconductivity in twisted graphene bilayers, Proc. Natl. Acad. Sci. USA **115**, 13174 (2018).

[21] N. Bultinck, E. Khalaf, S. Liu, S. Chatterjee, A. Vishwanath, and M. P. Zaletel, Ground State and Hidden Symmetry of Magic-Angle Graphene at Even Integer Filling, Phys. Rev. X **10**, 031034 (2020).

[22] Y. Alavirad and J. D. Sau, Ferromagnetism and its stability from the one-magnon spectrum in twisted bilayer graphene, Phys. Rev. B **102**, 235123 (2020).

[23] J. Liu and X. Dai, Theories for the correlated insulating states and quantum anomalous Hall effect phenomena in twisted bilayer graphene, Phys. Rev. B **103**, 035427 (2021).

[24] Y. Zhang, K. Jiang, Z. Wang, and F. C. Zhang, Correlated insulating phases of twisted bilayer graphene at commensurate filling fractions: a Hartree-Fock study, Phys. Rev. B **102**, 035136 (2020).

[25] J. Kang and O. Vafek, Non-Abelian Dirac node braiding and near-degeneracy of correlated phases at odd integer filling in magic angle twisted bilayer graphene, Phys. Rev. B **102**, 035161 (2020).

[26] K. Hejazi, X. Chen, and L. Balents, Hybrid Wannier Chern bands in magic angle twisted bilayer graphene and the quantized anomalous Hall effect, Phys. Rev. Res. **3**, 013242 (2021).

[27] T. Soejima, D. E. Parker, N. Bultinck, J. Hauschild, and M. P. Zaletel, Efficient simulation of moiré materials using the density matrix renormalization group, Phys. Rev. B **102**, 205111 (2020).

[28] J. Kang and O. Vafek, Strong Coupling Phases of Partially Filled Twisted Bilayer Graphene Narrow Bands, Phys. Rev. Lett. **122**, 246401 (2019).

[29] K. Seo, V. N. Kotov, and B. Uchoa, Ferromagnetic Mott State in Twisted Graphene Bilayers at the Magic Angle, Phys. Rev. Lett. **122**, 246402 (2019).

[30] O. Vafek and J. Kang, Renormalization Group Study of Hidden Symmetry in Twisted Bilayer Graphene with Coulomb Interactions, Phys. Rev. Lett. **125**, 257602 (2020).

[31] B. A. Bernevig, B. Lian, A. Cowsik, F. Xie, N. Regnault, and Z. D. Song, Twisted bilayer graphene. V. Exact analytic many-body excitations in Coulomb Hamiltonians: Charge gap, Goldstone modes, and absence of Cooper pairing, Phys. Rev. B **103**, 205415 (2021).

[32] B. A. Bernevig, Z. D. Song, N. Regnault, and B. Lian, Twisted bilayer graphene. III. Interacting Hamiltonian and exact symmetries, Phys. Rev. B **103**, 205413 (2021).

[33] N. Marzari and D. Vanderbilt, Maximally localized generalized Wannier functions for composite energy bands, Phys. Rev. B **56**, 12847 (1997); N. Marzari, A. A. Mostofi, J. R. Yates, I. Souza, and D. Vanderbilt, Maximally localized Wannier functions: Theory and applications, Rev. Mod. Phys. **84**, 1419 (2012).

[34] J. Kang, B. A. Bernevig, and O. Vafek, Cascades between light and heavy fermions in the normal state of magic angle twisted bilayer graphene, arXiv:2104.01145.

[35] A local spin-valley U(4) symmetry was first identified numerically in Ref. [28]; the detailed connection to this symmetry is left for a future publication.

[36] S. Becker *et al.*, Mathematics of magic angles in a model of twisted bilayer graphene, arXiv:2008.08489.

[37] K. Hejazi, C. Liu, H. Shapourian, X. Chen, and L. Balents, Multiple topological transitions in twisted bilayer graphene near the first magic angle, Phys. Rev. B **99**, 035111 (2019).

[38] J. Wang, Y. Zheng, A. J. Millis, and J. Cano, Chiral approximation to twisted bilayer graphene: Exact intra-valley inversion symmetry, nodal structure and implications for higher magic angles, Phys. Rev. Res. **3**, 023155 (2021).

[39] N. Bultinck, S. Chatterjee, and M. P. Zaletel, Mechanism for Anomalous Hall Ferromagnetism in Twisted Bilayer Graphene, Phys. Rev. Lett. **124**, 166601 (2020).

[40] E. Khalaf, N. Bultinck, A. Vishwanath, and M. P. Zaletel, Soft modes in magic angle twisted bilayer graphene, arXiv:2009.14827.

[41] X. Liu, Z. Wang, K. Watanabe, T. Taniguchi, O. Vafek, and J. Li, Tuning electron correlation in magic-angle twisted bilayer graphene using Coulomb screening, Science **371**, 1261 (2021).